

# Formation of Secondary Brown Carbon in Biomass Burning Aerosol Proxies through NO<sub>3</sub> Radical Reactions

Chunlin Li,<sup>†,∇</sup> Quanfu He,<sup>†,∇,Ⓛ</sup> Anusha Priyadarshani Silva Hettiyadura,<sup>‡</sup> Uwe Käfer,<sup>§,Ⓛ</sup> Guy Shmul,<sup>⊥</sup> Daphne Meidan,<sup>†</sup> Ralf Zimmermann,<sup>§,Ⓛ</sup> Steven S. Brown,<sup>#,★</sup> Christian George,<sup>◆,Ⓛ</sup> Alexander Laskin,<sup>‡,Ⓛ</sup> and Yinon Rudich<sup>\*,†,Ⓛ</sup>

<sup>†</sup>Department of Earth and Planetary Sciences, Weizmann Institute of Science, Rehovot 76100, Israel

<sup>‡</sup>Department of Chemistry, Purdue University, West Lafayette, Indiana 47907, United States

<sup>§</sup>Joint Mass Spectrometry Centre, University of Rostock, Dr.-Lorenz-Weg 2, 18059 Rostock, Germany

<sup>Ⓛ</sup>Joint Mass Spectrometry Centre, Cooperation Group “Comprehensive Molecular Analytics” (CMA), Helmholtz Zentrum München, Ingolstädter Landstrasse 1, 85764 Neuherberg, Germany

<sup>⊥</sup>Department of Chemical Research Support, Weizmann Institute of Science, Rehovot 76100, Israel

<sup>#</sup>Chemical Science Division, NOAA Earth System Research Laboratory (ESRL), Boulder, Colorado 80305, United States

<sup>★</sup>Department of Chemistry, University of Colorado, Boulder, Colorado 80309-0215, United States

<sup>◆</sup>Univ Lyon, Université Claude Bernard Lyon 1, CNRS, IRCÉLYON, F-69626, Villeurbanne, France

## Supporting Information

**ABSTRACT:** Atmospheric brown carbon (BrC) is an important contributor to the radiative forcing of climate by organic aerosols. Because of the molecular diversity of BrC compounds and their dynamic transformations, it is challenging to predictively understand BrC optical properties. OH radical and O<sub>3</sub> reactions, together with photolysis, lead to diminished light absorption and lower warming effects of biomass burning BrC. The effects of night-time aging on the optical properties of BrC aerosols are less known. To address this knowledge gap, night-time NO<sub>3</sub> radical chemistry with tar aerosols from wood pyrolysis was investigated in a flow reactor. This study shows that the optical properties of BrC change because of transformations driven by reactions with the NO<sub>3</sub> radical that form new absorbing species and lead to significant absorption enhancement over the ultraviolet–visible (UV–vis) range. The overnight aging increases the mass absorption coefficients of the BrC by a factor of 1.3–3.2 between 380 nm and 650 nm. Nitrated organic compounds, particularly nitroaromatics, were identified as the main products that contribute to the enhanced light absorption in the secondary BrC. Night-time aging of BrC aerosols represents an important source of secondary BrC and can have a pronounced effect on atmospheric chemistry and air pollution.



## 1. INTRODUCTION

Particles emitted from biomass burning (BB) undergo long-range atmospheric transport and significantly influence atmospheric chemistry, climate, and human health.<sup>1,2</sup> Under global warming scenarios, the number and intensity of wild fires are expected to increase, as has been recently shown.<sup>3</sup> The climatic effects of BB aerosols due to interactions with solar radiation are directly related to their intrinsic light-absorbing properties. However, unlike the well-established absorption by black carbon,<sup>4</sup> the optical properties of the brown carbon organic fraction in BB aerosols (BB-BrC) are poorly characterized, because of their highly complex chemical composition and the transformations that they undergo upon atmospheric processing.<sup>5,6</sup> Tar balls, which are common products of wood pyrolysis, were found in significant concentrations in fire emissions.<sup>7–9</sup> Tar aerosols from biomass burning absorb light over a wide portion of the ultraviolet–

visible (UV–vis) spectrum, implying that they may have substantial influences on climate and atmospheric chemistry, thus making them a suitable proxy for BB-BrC.<sup>10,11</sup> The extent of climate forcing by tar aerosols is dependent on their light-absorption properties, which are inherently related to their chemical composition and subsequent atmospheric transformations.<sup>10,12</sup>

Previous ambient and laboratory studies indicated that absorption associated with BB-BrC decays during the daytime with a half lifetime of ~10 h.<sup>13,14</sup> In the atmosphere, BrC undergo chemical processes, including OH and ozone-driven photochemical reactions during the day and oxidation by NO<sub>3</sub>

**Received:** September 18, 2019

**Revised:** November 12, 2019

**Accepted:** November 15, 2019

**Published:** November 15, 2019

radicals at night. These aging processes lead to chemical modifications of the aerosols with different effects on climate, air quality, and health. Many studies have investigated the changes in the chemical composition and light absorption properties of BrC with an emphasis on the roles of atmospheric OH radical and O<sub>3</sub> reactions, together with photolysis on the bleaching of BB-BrC aerosols.<sup>10,15–17</sup> In contrast, an enhancement in light absorption and the formation of chromophores in BB-BrC aerosols in ambient fire plumes were observed in samples collected at night or/and in the early morning. These observed optical changes were attributed to overnight aging processes.<sup>18–20</sup>

The reaction kinetics of NO<sub>3</sub> radicals with organic aerosol components are substantially slower and their surface uptake coefficients can be several orders lower than those of OH radicals.<sup>21,22</sup> However, the high atmospheric concentrations and the rapid rate of NO<sub>3</sub> radical production make its heterogeneous oxidation atmospherically important.<sup>21–23</sup> Numerous nitrated organic compounds have been identified in ambient BB aerosols and in anthropogenic organic aerosols. These compounds can significantly modify the optical properties and mass of BrC aerosols after undergoing reactions overnight.<sup>19,20,24</sup> A few previous studies have investigated the chemical kinetics and reaction pathways of NO<sub>3</sub> radicals with BB-BrC surrogates.<sup>25–27</sup> However, the aging of primary BB-BrC by NO<sub>3</sub> radical chemistry and the related composition-specific optical changes have not been reported.

The absorption properties of BB-BrC aerosols can be attributed to specific chemical-structural features or types of chromophores. Observations suggest that the common assumption of a monotonic decrease in BrC aerosol absorption with increasing wavelength does not always hold, because of absorption bands.<sup>18,19</sup> In addition, the commonly used method of measuring the absorption of bulk extractable BrC in solution may not fully account for particulate BrC absorption, because of the properties of the particles (such as aerosol geometry, size, phase, composition, and mixing state), which must be adequately studied, in addition to absorptions of BrC compounds in solutions.<sup>19,28</sup> Furthermore, *in situ* measurements of the aerosols' optical constants (e.g., extinction, scattering, and absorption coefficients) by cavity ring-down spectroscopy (CRDS), nephelometry, and photoacoustic spectrometry (PAS) at a few discrete wavelengths cannot capture the fine structures that influence particle absorption. Therefore, extinction measurements and refractive index (RI) determination over a wide spectral range by broadband instruments, such as a broadband cavity-enhanced spectrometry (BBCES) system, offer more direct and complete information on the optical properties of aerosols and their possible climatic and photochemical impacts.<sup>5,18,29</sup>

The identification of the molecular chromophores in BB-BrC remains challenging, because of the complexity of both the chromophores themselves and the chemical matrix. To date, the majority of the compounds in the BB-BrC mixture are still not characterized. Selected classes of compounds that contribute to BrC absorption have been identified, and these include aromatic/phenolic species, humic-like substances, heteroatom-containing high-molecular-weight organic species, and oligomeric derivatives of these compounds.<sup>19,30–32</sup> Of these, the semipolar and nonpolar absorbing compounds account for a significant proportion of the light absorption by BB-BrC, although they contribute only a small fraction of the mass.<sup>33,34</sup> The polarity of these constituents can influence their fate in the

atmosphere, including atmospheric chemical processes, and more importantly, their physical behavior in deposition and cloud condensation nuclei (CCN) activity.<sup>35,36</sup>

In this study, proxies for primary BB-BrC aerosols with different chemical polarities were generated in the laboratory from tar products obtained from wood pyrolysis.<sup>10,37</sup> The heterogeneous reactions of nebulized wood tar aerosols with NO<sub>3</sub> radicals under dark conditions were studied in an aerosol flow tube reactor, to simulate night-time aging. The complex broadband RIs for fresh and aged wood tar aerosols were determined over a wide spectral range (315–650 nm) and were linked to changes in chemical composition as characterized by online and offline mass spectrometry. The primary and secondary BrC chromophores in the fresh and aged wood tar aerosols were identified. The study uniquely shows the formation of a secondary BrC component via this chemistry and elucidates the mechanisms of these transformations.

## 2. MATERIALS AND METHODS

**2.1. Wood Tar Particle Generation.** The procedure for wood tar generation follows the work of Tóth et al.<sup>37</sup> and Li et al.<sup>10</sup> and is described in the Supporting Information (SI) (section S1). Briefly, commercial wood pellets (Hallingdal Trepellets) for domestic and power-plant usage were pyrolyzed to simulate the biofuel burning process. The wood tar formed by pyrolysis was collected and fractionated into three subfractions, based on the polarities of the constituents, using appropriate solvents: polar (water-soluble), moderately polar (acetonitrile-soluble), and nonpolar (dichloromethane/hexane 50/50 v/v mixture-soluble) extractions. The nonpolar wood tar extraction was dried via rotary evaporation and redissolved in a mixture of acetonitrile and methanol (50/50, v/v). Particles were generated via nebulization of these wood tar fractions, following heat shock, to mimic the fire escape process and compact the particles. The particles then passed through a denuder to remove remaining solvents. All the solvents (e.g., acetonitrile, methanol, dichloromethane, and hexane) were used as received with a purity of ≥99.9% (Sigma–Aldrich).

**2.2. Flow Tube Experiments.** The heterogeneous reactions of wood tar aerosols with NO<sub>3</sub> radicals in the presence of NO<sub>2</sub> and O<sub>2</sub> were conducted in an aerosol flow reactor (AFR) with N<sub>2</sub>O<sub>5</sub> as the source of NO<sub>3</sub> radicals. Gaseous N<sub>2</sub>O<sub>5</sub> was released from cold-trapped crystalline N<sub>2</sub>O<sub>5</sub> and NO<sub>3</sub> radicals formed via thermal decomposition. The initial N<sub>2</sub>O<sub>5</sub> and NO<sub>3</sub> radical concentrations were detected by a heated cavity ring-down spectrometry (CRDS) system (operating at 662 nm) using NO titration. By varying the initial mixing ratios of N<sub>2</sub>O<sub>5</sub> and NO<sub>3</sub> radicals, various oxidation levels of the wood tar aerosols were achieved. For descriptions of the AFR and N<sub>2</sub>O<sub>5</sub>–NO<sub>3</sub> detection, see the SI (sections S2 and S3).

**2.3. Wood Tar Particle Characterization.** The optical and chemical transformations of wood tar particles following NO<sub>3</sub> radical reactions were studied. Fresh and NO<sub>3</sub>-aged dry particles were scanned with a scanning mobility particle sizer (SMPS, TSI) and size-selected using an aerodynamic aerosol classifier (AAC, Cambustion, U.K.). The extinction cross sections ( $\sigma_{\text{ext}}$ ) of the monodisperse wood tar particles in the continuous wavelength ranges of 315–355 nm and 380–650 nm were measured via a BBCES system, in combination with a condensation particle counter (CPC, TSI). The values of the complex refractive index ( $\text{RI} = n + ik$ , where the real part ( $n$ ) and the imaginary part ( $k$ ) indicate scattering and absorption, respectively) were retrieved based on Mie–Lorenz scattering

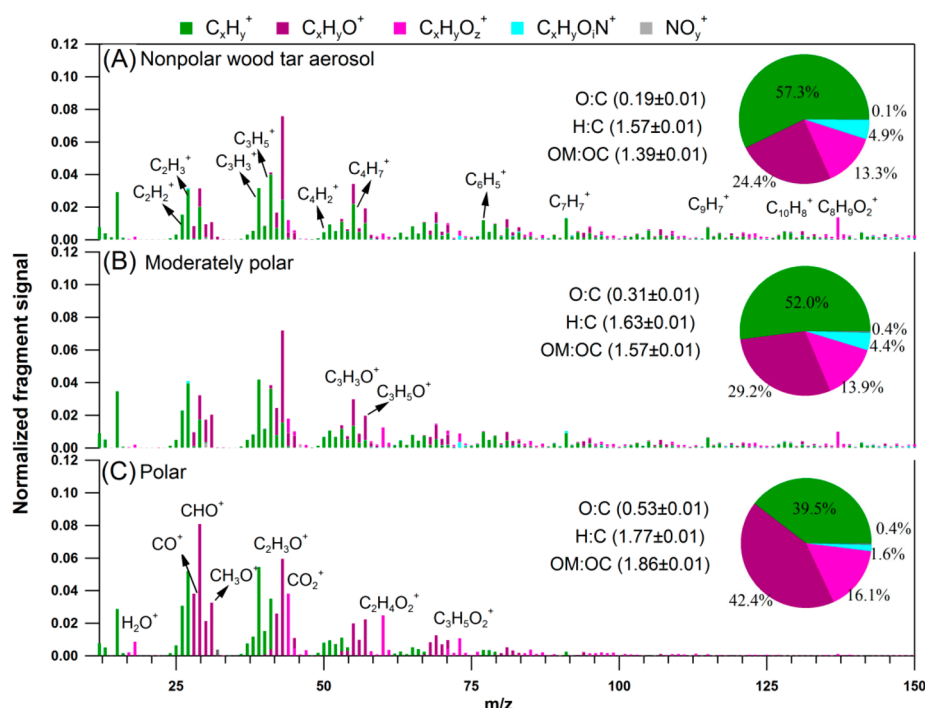


**Figure 1.** HR-ToF-AMS spectra of nonpolar, moderately polar, and polar wood tar aerosols. Six ion groups were classified according to their elemental compositions:  $C_xH_y^+$  (green),  $C_xH_yO^+$  (purple),  $C_xH_yO_z^+$  (violet),  $C_xH_yO_iN^+$  (light blue), and  $NO_y^+$  (gray), where  $z > 1$ ,  $y \geq 1$ ,  $z \geq 1$ , and  $i \geq 0$ , respectively. The relative contributions of these fragment groups are displayed as insert pie charts. The ions  $O^+$ ,  $OH^+$  and  $H_2O^+$  are included in the  $C_xH_yO_z^+$  group. The intensities of the signals for fragments over 150 amu were negligible, and they are not shown.

with wavelength- and particle size-resolved extinction cross sections, assuming sphericity and homogeneous chemical composition for wood tar particles. In addition, an integrated photoacoustic spectrometry (PAS) and CRDS system directly measured the absorption ( $\sigma_{abs}$ ) and extinction cross sections ( $\sigma_{ext}$ ) of the dry particles at 404 nm, thereby constraining and verifying the BBCES RI retrievals.

The chemical modifications of the wood tar aerosol by reactions with  $NO_3$  were monitored online by a high-resolution time-of-flight aerosol mass spectrometry (HR-ToF-AMS, Aerodyne). The fresh and processed wood tar aerosols were also collected on different substrates for subsequent analysis: on cyclopore track etched membrane (polycarbonate membrane, 0.1  $\mu m$  porosity, 47 mm diameter, Whatman) for individual particle morphological imaging and elemental analysis by environmental scanning electron microscopy (ESEM) (Thermoscientific Quattro S), on polished KBr plates for functional groups characterization by Fourier transform infrared spectroscopy (FT-IR) (Thermo Scientific Nicolet 6700), and on Teflon filter (polytetrafluoroethylene (PTFE), 0.45  $\mu m$  porosity, 47 mm diameter, Whatman) for chemical characterization and chromophores identification using multimass spectrometric techniques, including two-dimensional gas chromatography coupled to electron impact ionization high-resolution multi-reflection time-of-flight mass spectrometry (ToF-MS) (GC  $\times$  GC/EI-HR-ToF-MS), electrospray ionization (ESI) coupled with a quadrupole time-of-flight tandem mass spectrometry ((-)ESI-Q-ToF-MS), high-performance liquid chromatography (HPLC) system coupled with a photodiode array detector (PDA) and a Q-Exactive HF-X HR-MS equipped with an ESI source (HPLC-PDA-(-)ESI/HRMS). Additional details of the optical and MS system operation and data analysis are presented in the SI (sections S4 and S5).

### 3. RESULTS AND DISCUSSION

#### 3.1. Chemical Characterization of Wood Tar Aerosol.

Laboratory-generated wood tar aerosols are a suitable proxy for primary biomass burning aerosols, because their physical and chemical characteristics are highly similar to those of ambient tar ball particles.<sup>7,38</sup> The produced wood tar aerosols are spherical particles with a homogeneous carbonaceous composition and median diameters in the range of 150–250 nm. The energy-dispersive X-ray (EDX) spectra indicate that they are mostly made of carbon and contain a small amount of oxygen. The nitrogen and sulfur signals were close to the background level (see Figure S1 in the SI). The EDX spectra is consistent with the HR-ToF-AMS measurements of organic elements in the same tar aerosols. The HR-ToF-AMS analysis provides the bulk chemical characteristics of the complex nonrefractory organic matter in the particles. From the overview shown in Figure 1, nonpolar wood tar aerosols contain a higher proportion of hydrocarbon-like ions ( $C_xH_y^+$ ). Oxygenated organic fragments ( $C_xH_yO^+$  and  $C_xH_yO_z^+$ ) comprise a larger fraction of the polar tar aerosols, indicated by higher O/C ratios. Nitrogen-containing fragments ( $C_xH_yO_iN^+$ ) account for 1.6%–4.9% of the total signals, indicating that fresh wood tar aerosols have a small portion of nitrogen-containing organic compounds (NOC), likely from the biomass fuel itself. NOC, especially N-heterocyclic alkaloids and amides (biogenic species naturally produced by plants), are abundant in BB emissions.<sup>31,39</sup> The primary components of fresh biomass burning organic aerosols can undergo chemical changes during atmospheric aging processes, leading to the incorporation of nitrogen into the organic constituents in the form of nitro and nitrate functional groups.<sup>19,24</sup> The nitrate fraction in the fresh wood tar particles is negligible, and the ratios of the  $NO_2^+$  and  $NO^+$  signals ( $0.43 \pm 0.2$ ) in the particles are consistent with the ratio measured for

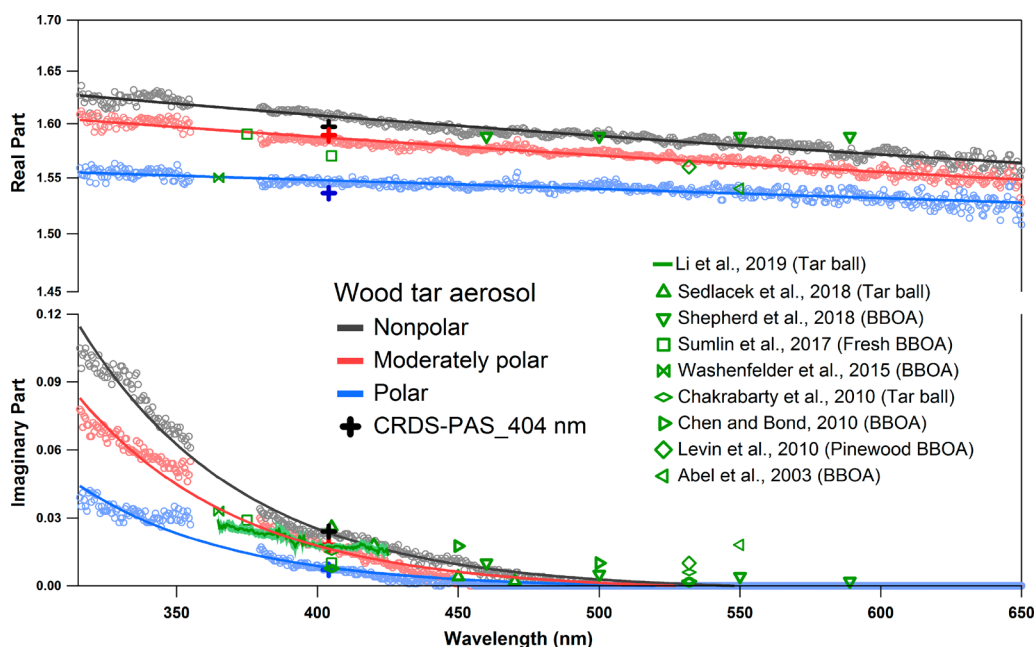


**Figure 2.** Complex broadband refractive index (RI) of fresh wood tar aerosols between 315 nm and 650 nm. The pale, unfilled dots are the retrieved RIs. The corresponding black, red, and blue solid lines are exponential (real part,  $n$ ) and power law fits (imaginary part,  $k$ ) of the RI values for nonpolar, moderately polar, and polar wood tar aerosols, respectively. The cross symbols indicate the CRDS–PAS-retrieved RIs at 404 nm, which are in good agreement with the retrieved BBCES. The error bars of each retrieved RI are not shown for clarity ( $\pm 0.006$  for the real part and  $\pm 0.003$  for the imaginary part, on average). Open symbols in green indicate literature values of RIs.

pure  $\text{NH}_4\text{NO}_3$  particles, suggesting that the majority of nitrates in the unprocessed wood tar particles are present in their inorganic form.

Although the parent ion peaks are often lost in electron impact (EI) ionization, some molecular-level information can be inferred from the fragments detected by AMS. Specifically,  $\text{C}_2\text{H}_4\text{O}_2^+$  and  $\text{C}_3\text{H}_5\text{O}_2^+$  are characteristic fragments of the EI ionization of anhydrous sugars (e.g., biomarkers including levoglucosan and mannosan), although  $\text{C}_2\text{H}_4\text{O}_2^+$  may also originate from rearrangement of fatty acids. Together, these two ions are commonly used for classifying biomass burning aerosols by AMS in the field.<sup>40</sup> Prominent signals for these two ions were detected in the higher polarity wood tar aerosols, especially in the water-soluble tar aerosols. The  $\text{CO}_2^+$  fragment originates from the fragmentation of acids, esters, and peroxides.  $\text{C}_2\text{H}_3\text{O}^+$  is a typical fragment of ketones and aldehydes.<sup>41</sup> The relatively high intensities of  $\text{CO}_2^+$  and  $\text{C}_2\text{H}_3\text{O}^+$  in the AMS spectra of polar tar aerosols suggest that carboxyl- and carbonyl-containing compounds are abundant in the polar fraction. Strong signals for other characteristic ions (e.g.,  $\text{C}_6\text{H}_5^+$ ,  $\text{C}_7\text{H}_7^+$ ,  $\text{C}_{10}\text{H}_8^+$ , and  $\text{C}_8\text{H}_9\text{O}_2^+$ ) that correspond to aromatic hydrocarbons and phenols were observed in the mass spectra of the moderately polar and nonpolar wood tar aerosols, indicating that these particles contain aromatic species.<sup>42,43</sup>

Two-dimensional gas chromatography coupled to mass spectrometry (GC  $\times$  GC-MS) allows the separation and identification of parent compounds and isomers that cannot be resolved using AMS. Here, the moderately polar tar aerosol, treated as a mixture of polar and nonpolar wood tar components, was characterized via GC  $\times$  GC/EI-HR-ToF-MS. The chromatogram (Figure S2 in the SI) shows that wood tar aerosols contain a wide variety of alkanes (C11–C25), naphthenes, naphthalenes, amides, abietic acid derivatives, and anhydrous sugars, as well as aromatic species bearing hydroxy, methoxy, carbonyl, and carboxyl functional groups. High

content of alkylphenols, methoxyphenols, and benzoic acids (e.g., dimethylphenol, guaiacol, syringol, syringaldehyde, vanillin, and acetovanillone) were detected in the moderately polar tar particles. Abietic acid and amides are surrogates of BB products, and anhydrous sugars are characteristic products of lignin pyrolysis.<sup>44,45</sup> These chemicals represent high proportions of the compounds found in ambient and laboratory fire emissions; thus, wood tar aerosols are a suitable proxy for organic aerosols from biomass burning (BBOA).<sup>37,45</sup>

**3.2. Optical Features of Wood Tar Aerosols.** The retrieved complex RIs of the fresh wood tar aerosols are shown in Figure 2, and these results provide the first broadband insight into the intrinsic optical properties of BB-BrC proxy particles. The RIs at a single wavelength of 404 nm were independently derived with a PAS-CRDS system (black crosses in Figure 2), and they fit well with the BBCES retrievals. The results are summarized in Table S1 in the SI. The wavelength-dependent imaginary RI values in Figure 2 show that light absorption by wood tar particles is strong at short wavelengths and extends into the visible range up to  $\sim 500$  nm, thus coinciding with the maximal intensity of the incoming solar radiation. The scattering (real part) by the wood tar particles has a more moderate wavelength dependence. Although there are only a small number of studies on the optical properties of tar particles, the RI values derived here are consistent with those from discrete/narrow band measurements of BB-BrC aerosols from both field and laboratory studies, as also shown in Figure 2.<sup>7,10,13,46–51</sup>

The retrieved RIs are closely related to the particles' chemical composition. Both the real and imaginary parts of the RI decrease with the polarity of the wood tar material. At 404 nm, the retrieved RI values are  $(1.545 \pm 0.007) + (0.008 \pm 0.003)i$ ,  $(1.584 \pm 0.005) + (0.016 \pm 0.001)i$ , and  $(1.608 \pm 0.002) + (0.023 \pm 0.002)i$  for the polar, moderately polar, and nonpolar wood tar aerosols, respectively. At this wavelength, the single

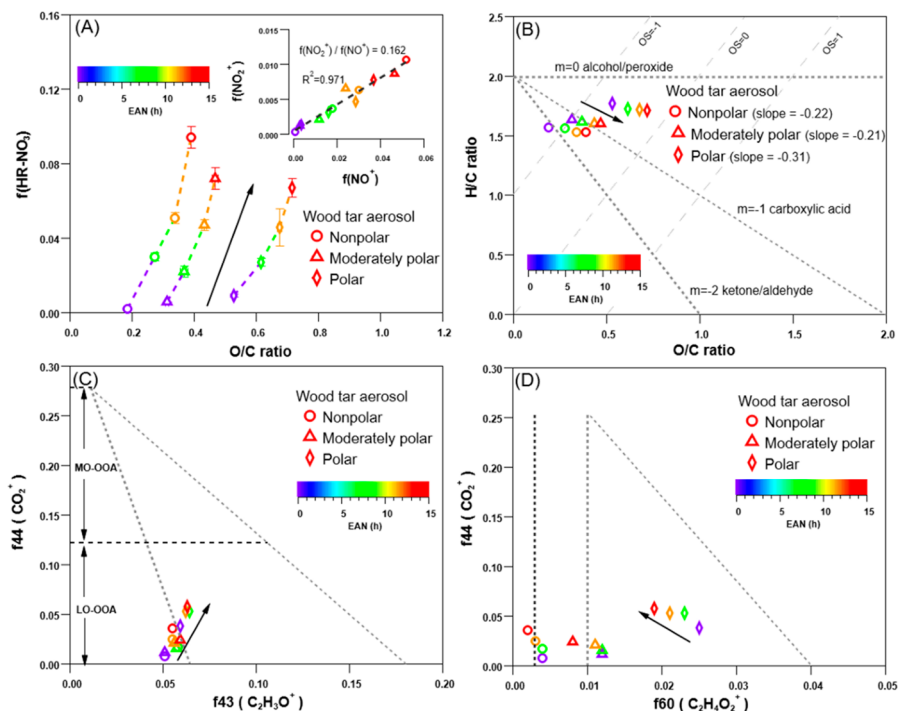


**Figure 3.** HR-ToF-AMS results of wood tar aerosols following  $\text{NO}_3$  radical aging. The color of the symbols indicate the equivalent ambient  $\text{NO}_3$  radical aging time. (A) Nitrate formation as a function of the O/C ratio and oxidation. The inserted graph shows the linear regression of the characteristic nitrate fragments ( $\text{NO}^+$  vs  $\text{NO}_2^+$ ). (B) Van Krevelen diagram showing the H/C ratio as a function of the O/C ratio. The observed dashed lines with slope  $m$  denote changes in functional groups upon oxidation, and the oxidation state (OS) line describes the change in the oxidation state of carbon for the aerosols. (C) Plot of  $f_{44}$  vs  $f_{43}$  inside the region in the triangle inscribed by the dashed lines, indicating the ambient oxygenated organic aerosol (OOA), from Ng et al.<sup>41</sup> Ambient less-oxidized OOA (LO-OOA) and more-oxidized OOA (MO-OOA) are mainly found in the lower and upper parts of the triangular region, respectively. (D) Plot of  $f_{44}$  vs  $f_{60}$ . The nominal background value of  $f_{60}$  is  $\sim 0.3\%$  from AMS measurements along the vertical black dashed line. Ambient biomass burning organic aerosols commonly fall inside the triangular region defined by the gray dashed lines introduced by Cubison et al.<sup>40</sup>

scattering albedo (SSA) values for 250 nm wood tar particles were calculated based on Mie theory to be  $0.964 \pm 0.014$ ,  $0.938 \pm 0.007$ , and  $0.918 \pm 0.012$ . These values are consistent with the SSA values directly measured from CRDS-PAS at 404 nm (see Table S1). The mass absorption coefficient (MAC) is an alternative quantitative measure of the absorbing properties of bulk BrC aerosols. The MAC values were derived from the imaginary RI and the particle density (measured by comparing the aerodynamic and electrical mobility diameters; see the SI) via eq 1:

$$\text{MAC}_{(\lambda)} = \frac{4\pi k_{(\lambda)}}{\lambda \rho} \quad (1)$$

The values of  $\text{MAC}_{404}$  were estimated to be  $0.18 \pm 0.06$ ,  $0.42 \pm 0.03$ , and  $0.62 \pm 0.03 \text{ m}^2 \text{ g}^{-1}$  for the polar, moderately polar, and nonpolar wood tar particles, respectively. These values are in agreement with those of typical ambient BrC from biomass burning ( $0.2\text{--}1.1 \text{ m}^2 \text{ g}^{-1}$  at 405 nm).<sup>18</sup>

The absorption Ångström exponent (AAE) is often used to characterize the spectral dependence of the light absorption by aerosols and bulk materials. As mentioned, the AAE values deduced from normalized solution absorption may not accurately reflect the absorption properties of particles.<sup>19,52</sup> Otherwise, the AAE obtained from the particle absorption coefficients ( $\alpha_{\text{abs}}$ ) at two discrete wavelengths may also lead to a bias arising from the uncertainty of the limited arbitrary absorption coefficients. In this study, the AAE of wood tar absorption was determined from the linear regression fit to  $\ln(k)$

vs  $\ln(\lambda)$  in the continuous wavelength range of 315–450 nm by eq 2:

$$\text{AAE} = -\frac{\ln(\text{MAC}_{(\lambda)})}{\ln(\lambda)} = -\frac{\ln(k_{(\lambda)})}{\ln(\lambda)} + 1 \quad (2)$$

Different AAE values for polar ( $9.1 \pm 0.7$ ), moderately polar ( $9.4 \pm 0.7$ ), and nonpolar ( $7.8 \pm 0.6$ ) wood tar aerosols were determined from imaginary  $k$  distributions. These values are within the typical ranges of AAE values for ambient and laboratory BB-BrC.<sup>30,49</sup> The lower AAE values of the nonpolar wood tar particles indicate a weaker spectral dependence of the light absorption than those of polar particles, which can be attributed to the higher proportion of  $\text{sp}^2$  hybridized carbon in the nonpolar particles.<sup>30</sup>

According to the chemical characterization, the aromatic and the heteroatom (N and O)-containing polar functional groups may explain the light absorptivity of wood tar particles.<sup>51</sup> In addition, conjugated systems can form complexes between aromatic and oxygenated functional groups (carbonyl and hydroxyl), which may absorb visible light.<sup>52,53</sup> The relatively high aromaticity, high chromophore content, and less-oxidized chemical composition lead to a stronger absorption capacity for the moderately polar and nonpolar wood tar particles. A similar result was also observed in HULIS, where their imaginary RIs increase linearly with the aromatic content and generally decreased with the O/C ratio.<sup>53–55</sup>

**3.3. Chemical Transformation via  $\text{NO}_3$  Radical Reactions.** Controlled  $\text{NO}_3$  radical reactions with wood tar particles

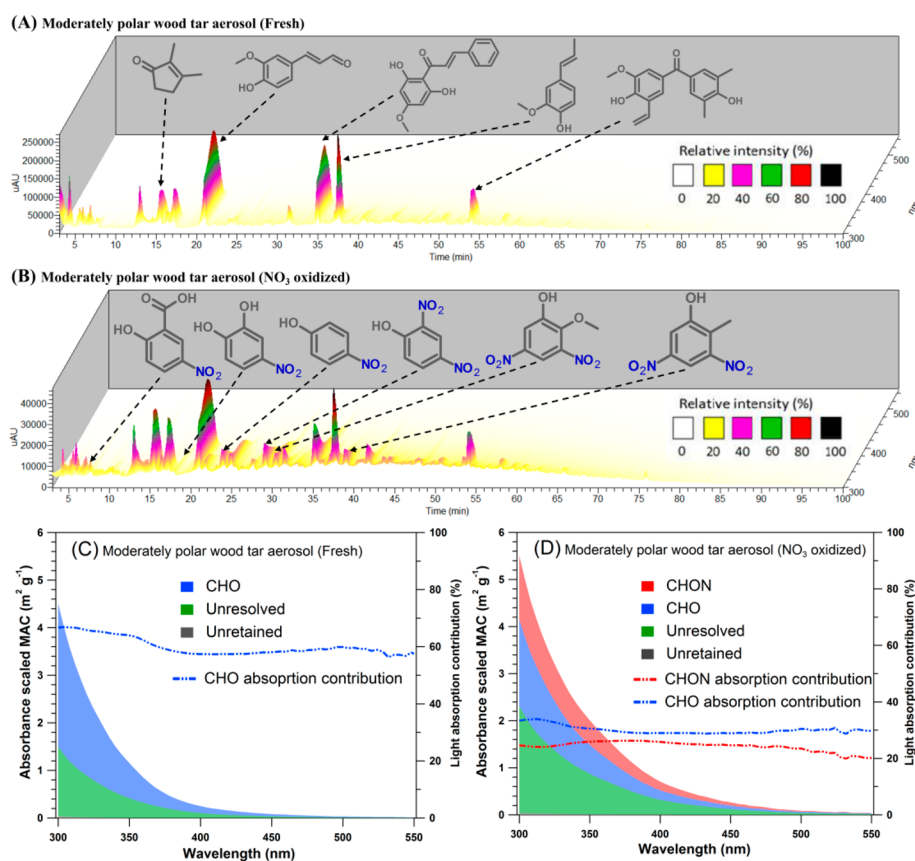


**Figure 4.** HPLC-PDA/(-)ESI-HRMS results for fresh and aged (13.3 h equivalent ambient  $\text{NO}_3$  reactions) moderately polar wood tar aerosol extracts. Panels (A) and (B) show the elution chromatograms. The colors indicate the absorbance intensity recorded by the PDA detector. The tentative molecular structures of some of the absorbing chromophores were inferred from PDA/ESI-HRMS. Panels (C) and (D) show plots of the absorption contributions of different fractions of chromophores classified based on their elemental features (CHON represents the total identified light-absorbing nitro-compounds and organonitrates, and the remaining resolved chromophores are included in CHO). The total UV-vis spectra recorded by the PDA detector were scaled to match the imaginary RI-derived MAC values of the particle at 330 nm. The negligible unretained chromophores are those species that were not retained on the column. Unresolved chromophores are chemicals that separated on the column, but their concentrations were too low for reliable characterization.

were conducted in an AFR under dry and dark conditions. The loss of oxidants in the AFR experiments was simulated by initiating a chemical box model that assesses the  $\text{NO}_3$  radical and  $\text{N}_2\text{O}_5$  particle surface uptake. Moreover, the extent of wood tar aerosol evolution in the AFR was adjusted to simulate ambient smoke particles aging due to  $\text{NO}_3$  radical and  $\text{N}_2\text{O}_5$  reactions, and was termed as “equivalent ambient night aging time” (EAN). A detailed description of the model is provided in the SI (section S6); the parameters and results are summarized and displayed in Tables S2–S4 and Figures S3 and S4 in the SI. From the chemical box model, we estimate that the reactive uptake of  $\text{NO}_3$  radicals by wood tar aerosols exceeds the  $\text{N}_2\text{O}_5$  uptake by one or two orders of magnitude (see Figure S4). Therefore, we concluded that  $\text{NO}_3$  radical reactions are the dominant oxidation pathway of wood tar aerosols, although  $\text{N}_2\text{O}_5$  can also be a nitrating agent at the dehydrated organic surface. By varying the initial mixing ratios between  $\text{N}_2\text{O}_5$  and the wood tar aerosols, EAN values of 8.3–13.3 h were achieved, thus simulating an overnight aging by  $\text{NO}_3$  and  $\text{N}_2\text{O}_5$  chemistry of smoke particles.

Oxidative aging modifies the chemical composition of the BB-BrC aerosols. Figure 3 illustrates the evolution of the characteristic fragments and functional groups of the bulk aerosol upon reactions with  $\text{NO}_3$  radical. A substantial amount of nitrate was generated in the  $\text{NO}_3$ -processed wood tar aerosol

based on the AMS results shown in Figure 3A. This result was also confirmed by EDX spectra, which show that nitrogen was added to individual aged tar particles (see Figure S1). The average nitrate contribution monotonically increased from negligible levels up to  $\sim 8$  wt % after simulating an EAN value of 13.3 h. The  $\text{NO}_2^+/\text{NO}^+$  ratios decreased from an initial value of 0.43 to 0.16 after  $\text{NO}_3$  radical aging, implying that the nitrates formed are mainly organic species ( $-\text{ONO}_2$  and/or  $-\text{NO}_2$ ) rather than inorganic salts ( $\text{NO}_3^-$ ).<sup>56</sup> The elemental ratios in the processed wood tar aerosols were calculated accounting for the organic nitrate contribution. The resulting H/C and O/C ratios are plotted in Figure 3B and summarized in Table S5 in the SI. A higher O/C ratio and a lower H/C ratio indicate oxygen addition and the loss of hydrogen in the  $\text{NO}_3$  radical reactions with wood tar particles, leading an overall increase in the carbon oxidation state of the aerosol ( $\overline{\text{OS}} \approx 2 \times \text{O/C} - \text{H/C} - 5 \times \text{N/C}$ ).<sup>57</sup>

The fractions of  $\text{C}_2\text{H}_3\text{O}^+$  ( $f_{43}$ ) and  $\text{CO}_2^+$  ( $f_{44}$ ) are strongly correlated with the aging extent of the organic aerosols and with the physical properties of the particles, such as their volatility and hygroscopicity.<sup>40</sup> Both  $f_{43}$  and  $f_{44}$  increased with aging of the tar aerosols (Figure 3C), confirming the formation of organic carbonyl and carboxyl or/and peroxide derivatives. The increase in  $f_{44}$ , relative to  $f_{43}$  and organic nitrate formation, suggests that the aged wood tar aerosols are less volatile and may

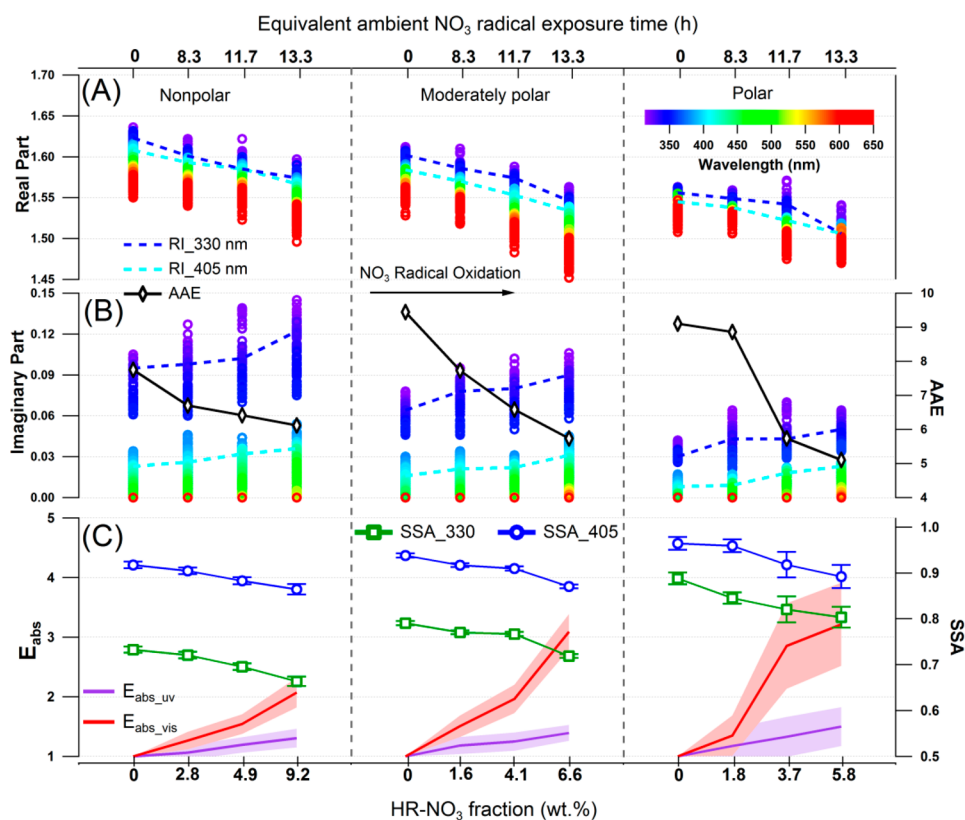


**Figure 5.** Optical modifications of wood tar aerosols due to reactions with  $\text{NO}_3$  radical. (A, B) Evolution of the broadband RIs, as a function of equivalent ambient  $\text{NO}_3$  radical aging time (EAN, top axis) and of the corresponding nitrate formation from the HR-ToF-AMS results (HR- $\text{NO}_3$ , bottom axis). The error bars for RIs, EAN, and HR- $\text{NO}_3$  are not presented for clarity; the detailed values are provided in the SI. Changes in the imaginary RI retrieved AAE values are displayed as solid black lines with diamond symbols. The two dashed lines indicate the RI values at 330 nm (indigo) and 405 nm (cyan). (C) Absorption enhancements ( $E_{\text{abs}}$ ) in the near-ultraviolet region of 315–355 nm ( $E_{\text{abs-UV}}$ , purple line and shaded area) and in the visible region of 380–450 nm ( $E_{\text{abs-vis}}$ , red line and shaded area) for wood tar aerosols, following  $\text{NO}_3$  radical exposures. SSA transformations for 250 nm wood tar particles at wavelengths of 330 and 405 nm were plotted as green squares and blue circles.

have higher CCN activity.<sup>26,40</sup> In the nonpolar and moderately polar tar aerosols,  $\text{NO}_3$  reacts with the aromatic compounds (e.g., methoxyphenols), decreasing the fractions of their characteristic fragments (e.g.,  $\text{C}_3\text{H}_3^+$ ,  $\text{C}_6\text{H}_5^+$ ,  $\text{C}_7\text{H}_7^+$ , and  $\text{C}_8\text{H}_9\text{O}_2^+$ ) (see Figures S5–S7 in the SI).<sup>42</sup> The  $\text{NO}_3$  oxidation also degrades the anhydrous sugars in the tar aerosol, resulting in the rapid decay of the  $\text{C}_2\text{H}_4\text{O}_2^+$  signal, as shown in Figure 3D. A growing number of studies have shown that levoglucosan has a short lifetime (0.7–2.2 days) in both photochemical reactions and night-time oxidation, suggesting that the concentration of levoglucosan may not be conserved during the transport of BB aerosols.<sup>58,59</sup>

Similarly, FT-IR spectra of moderately polar wood tar aerosols show that reactions with the  $\text{NO}_3$  radical resulted in nitration (Figure S8 in the SI). In addition to decreases in the  $-\text{OH}$  stretching and aliphatic  $-\text{C-H}$  stretching bands, which can be attributed to hydrogen-abstraction and hydrogen-transfer reactions, some infrared bands in the fingerprint region that are typical of the  $-\text{ONO}_2$  asymmetric stretch ( $1645\text{ cm}^{-1}$ ), the  $-\text{ONO}_2$  symmetric stretch ( $1280\text{ cm}^{-1}$ ), the  $\text{RO}-\text{NO}_2$  stretch ( $854\text{ cm}^{-1}$ ), and the  $\text{R}-\text{NO}_2$  stretch ( $1386$ ,  $1359$ , and  $1554\text{ cm}^{-1}$ ) of organic nitrate and nitro products were observed, and the intensities of these bands increase with  $\text{NO}_3$  exposure.<sup>60</sup> Considering the enrichment of PAHs, phenols, and methoxylated phenols in wood tar particles, the formation of  $\text{R}-\text{NO}_2$  occurs by  $\text{NO}_3$  radical-initiated reactions in the presence of  $\text{NO}_2$ . The enhanced absorbance band at  $\sim 1718\text{ cm}^{-1}$  suggests

the formation of carbonyl ( $\text{C}=\text{O}$ ) derivatives. The increased abundance of these moieties is also confirmed by the increases in  $f_{43}$  and  $f_{44}$  in the AMS results. The decrease in the intensity of the aromatic  $\text{C}=\text{C}$  stretch ( $1590$  and  $1515\text{ cm}^{-1}$ ) in the normalized IR spectra is additional evidence for the reactions of aromatic compounds through uptake of the  $\text{NO}_3$  radical.

The molecular modifications in  $\text{NO}_3$ -aged wood tar aerosols were also probed using ESI-HRMS operating in negative ion mode, because of its sensitive detection of polar compounds with acidic protons, specifically nitro-aromatics and phenols.<sup>61</sup> Molecular spectra were acquired for fresh and  $\text{NO}_3$  radical-aged moderately polar wood tar aerosols sample solutions, which infused directly into the ESI-HRMS. The elemental formulas were grouped and are compared in Figures S9 and S10, and Table S6, in the SI.  $\text{NO}_3$  radical reactions significantly altered the aerosols' molecular composition, with the average chemical formula changing from  $\text{C}_{18.6}\text{H}_{22.8}\text{O}_{5.8}\text{N}_{0.68}\text{S}_{0.07}$  to  $\text{C}_{20.6}\text{H}_{21.6}\text{O}_{9.7}\text{N}_{1.32}\text{S}_{0.02}$  after the equivalent of 13.3 h of aging with ambient  $\text{NO}_3$  radical. The increase in the average number of carbons and the overall molecular size may imply that oligomerization/functionalization processes are induced by the  $\text{NO}_3$  radical reactions, while the decrease in the number of hydrogens and the dramatic increase in oxygen, compared to nitrogen, in the average formula suggest hydrogen abstraction, nitration, and the incorporation of additional oxygens, leading to a substantial increase in the O/C ratio and the OS value. The  $\text{NO}_3$  radical reactions resulted in a large number of new

chemical products. Many of these chemicals, such as  $C_8H_7NO_5$ ,  $C_6H_5NO_4$ ,  $C_7H_7NO_4$ ,  $C_7H_5NO_5$ , and  $C_9H_9NO_6$ , have also been detected in BB-BrC aged overnight under ambient conditions.<sup>19,61</sup> In combination with the results of the GC × GC/EI-HR-ToF-MS in fresh tar particles, these products were tentatively assigned as nitrovanillin, nitrocatechol, nitroguaiacol, hydroxy-nitrobenzoic acid, and dimethoxy-nitrobenzoic acid, respectively. These compounds have been identified as the dominant BrC chromophores.<sup>19,61,62</sup> Moreover, the replacement of one or two additional hydrogens by nitro or nitrate functional groups was also common among identified compounds (e.g.,  $C_6H_4N_2O_{5-6}$ ,  $C_7H_{4-6}N_{2-3}O_{5-8}$ ,  $C_8H_{5-8}N_{2-3}O_{5-8}$ , and  $C_9H_{7-8}N_{2-3}O_{7-9}$ ), demonstrating that wood tar compounds can sequester reactive nitrogen oxides ( $NO_x$ ) to produce secondary BrC species. In addition, the significant reduction in  $C_6H_{10}O_5$  (glucose monomer) in Figure S9 in the SI further confirms the decomposition of sugars during the  $NO_3$  radical reactions, as observed by HR-ToF-AMS.

Figures 4A and 4B show the HPLC-PDA/(−)ESI-HRMS chromatograms of the unprocessed and  $NO_3$ -treated moderately polar wood tar extracts. More light-absorbing compounds were detected in the aged samples, and the major resolved chromophores correspond well with the chemical speciation shown in Figures S2 and S9. For example, in fresh samples, the major identified chromophores are phenols bearing methoxyl, carbonyl, or/and vinyl groups, e.g.,  $C_{10}H_{10}O_3$  and  $C_{10}H_{12}O_2$  (coniferyl aldehyde and eugenol, respectively). In  $NO_3$ -aged aerosols, the newly formed species with the formulas  $C_7H_5NO_5$ ,  $C_6H_3NO_{3-4}$ ,  $C_6H_4N_2O_5$ , and  $C_7H_6N_2O_6$  were tentatively identified as nitrosalicylic acid, nitrophenol/catechol, dinitrophenol, and dinitroguaiacol, respectively. Figures 4C and 4D show plots of the absorption efficiency and contributions of different fractions of chromophores classified based on their elemental compositions. The aging of wood tar aerosols via  $NO_3$  radical reactions modifies the composition of chromophores. The initial chromophores (CHO) were partly depleted and converted to nitrated chromophores (CHON) and other unresolved light-absorbing products, causing the aged particles to absorb more light in the 300–550 nm range.

The  $NO_3$  radical reaction pathways vary, depending on the chemical composition and the functional groups present. The initial  $NO_3$  radical may react with unsaturated carbon bonds to form nitro-oxy-alkyl radicals. These radicals subsequently react with oxygen to produce nitro-oxy-alkyl-peroxy radicals, which can undergo intramolecular reactions or react with  $NO_2$  or  $NO_3$  to generate hydroxyl nitrates, carbonyl nitrates, or thermally unstable nitro-oxy-peroxy-nitrates and nitro-oxy-peroxides.<sup>25,62</sup> Hydrogen abstraction by the  $NO_3$  radical occurs preferentially on alkanes, hydrocarbon-PAHs and species with carbonyl, carboxyl, and phenolic hydroxy groups prior to the reactions of  $NO_2$  and  $NO_3$  with the ensuing peroxy radicals.<sup>23,27</sup> On the basis of the identified parent compounds and reaction products, the reaction mechanisms of the different surrogates with  $NO_3$  radicals are proposed and summarized in Figure S11 in the SI.

**3.4. Absorption Enhancement of BrC via  $NO_3$  radical Reactions.** Figure S12 in the SI shows that the chemical composition does not change with particle size following the reactions. This suggests that the  $NO_3$  chemistry is not limited to the surface of the wood tar aerosols. The complex RIs for wood tar aerosols, as a function of  $NO_3$  radical exposure (top axis) and the production of the corresponding nitrates, based on HR-ToF-AMS measurements (bottom axis), are displayed in Figure 5. Clearly, the reactions of  $NO_3$  with the wood tar components

changed both the scattering and absorption properties of the aerosols (see Figure 5, as well as Figure S13 in the SI), and lead to the formation of new chromophores that enhance the absorption. A monotonic decrease in the real part of the RI upon increasing  $NO_3$  radical exposure was observed in Figure 5A. Based on the empirical Lorentz–Lorenz relation that positively correlate the real RI with the mean polarizability ( $\alpha$ ) and the molecular volume (or the density divided by the molecular weight,  $\rho/MW$ ) of a substance,<sup>63,64</sup> an appreciable decrease in light scattering is expected for aged wood tar particles, according to eq 3:

$$\frac{n^2 - 1}{n^2 + 2} = \frac{N_A \alpha \rho}{3MW} \quad (3)$$

Taking the average formula from the (−)ESI-HRMS results to represent the bulk chemical composition of the wood tar particles, the mean polarizability for the aerosol can be estimated based on their elemental features.<sup>63,64</sup> The  $NO_3$  radical oxidation indeed increased the wood tar aerosols' mean polarizability and molecular weight, while it decreased the density of the particles (Table S1), ultimately resulting in lower real RIs, as projected by the Lorentz–Lorenz relation.

A substantial enhancement in absorption was detected for wood tar aerosols following reactions with the  $NO_3$  radical. The imaginary RI values increased and extended to longer wavelengths in the visible region (Figure 5B). The average imaginary RIs at 330 and 405 nm increased by  $0.008 \pm 0.001$  and  $0.005 \pm 0.001$  over the course of overnight equivalent ambient  $NO_3$  radical aging. The particle absorption coefficients were integrated over the measured wavelength range to compare the absorption changes for the processed wood tar via eq 4:

$$E_{\text{abs}} = \frac{\int_{\lambda} \text{MAC}_{(\lambda)} d\lambda}{\int_{\lambda} \text{MAC}_{(\lambda)_0} d\lambda} \quad (4)$$

As shown in Figure 5C, a larger absorption enhancement occurred in the visible range ( $E_{\text{abs,vis}}$  380–650 nm) than the ultraviolet region ( $E_{\text{abs,uv}}$  315–355 nm), and  $E_{\text{abs}}$  was higher in the aged moderately polar and polar wood tar aerosols. After  $NO_3$  radical oxidation for EAN = 13.3 h, the light absorption in the visible region increased by a factor of 2.0–3.2 and increased by 40%, on average, in the UV region for wood tar particles. Consequently, the average SSA for wood tar particles with an atmospherically relevant size of 250 nm was reduced from  $0.80 \pm 0.08$  to  $0.73 \pm 0.07$  at 330 nm and from  $0.94 \pm 0.02$  to  $0.88 \pm 0.02$  at 405 nm.

The positive correlation between the imaginary RI/ $E_{\text{abs}}$  and  $NO_3$  radical exposure (Figure 5) and chromophore speciation in aged wood tar aerosols (Figure 4) indicates that nitrated organic compounds, especially nitro-aromatics, are important secondary chromophores and are the main species responsible for the absorption enhancement in aged wood tar particles upon  $NO_3$  aging.<sup>19,31</sup> Previous studies have found that the substitution of aromatic rings by nitro groups enhances and shifts their absorption to longer wavelengths ( $\lambda > 350$  nm),<sup>65</sup> consistent with this study. The AAE coefficients decreased with  $NO_3$  oxidation (Figure 5B), suggesting a lower wavelength dependence of light absorption for the aged wood tar aerosols. The imaginary RIs for  $NO_3$  radical-aged wood tar aerosols exhibit an apparent absorption band in the 400–450 nm range (Figure S12), which overlaps with the absorption peaks and shoulders that are characteristic of some specific nitrated aromatic

compounds (e.g.,  $C_6H_5NO_{3-5}$ ,  $C_7H_7NO_{4-5}$ , and  $C_{10}H_{13}NO_6$ ) that were detected by (–)ESI-HRMS.<sup>31,61</sup> Taken together, our results indicate that, unlike the photochemical bleaching of BB-BrC by the OH- and  $O_3$ -initiated reactions that occur during the daytime (and at low NO<sub>x</sub>), night-time aging by NO<sub>3</sub> radicals can significantly enhance the light absorption of biomass burning aerosols. This study confirms previous suggestions that NO<sub>3</sub> radical chemistry generates secondary BrC species through the formation of light-absorbing nitrated aromatic compounds, which enhance the overall light-absorbing properties of BrC.<sup>19,31</sup>

#### 4. ATMOSPHERIC IMPLICATION

Unlike the bleaching of BB-BrC via OH radical photochemistry and  $O_3$  oxidation reactions (at zero or low NO<sub>x</sub> concentrations) that occur during daylight, heterogeneous night-time reactions of NO<sub>3</sub> and N<sub>2</sub>O<sub>5</sub> lead to the formation of secondary brown carbon, which enhances their absorption. Consequently, the SSA of aged wood tar decreases. Nitrated products (e.g., organonitrate and nitro-aromatic species) are the primary new chromophores responsible for the absorption enhancement, suggesting that night-time NO<sub>3</sub> reactions can be an important source of secondary BrC in biomass burning plumes, especially when they interact with polluted air with high NO<sub>x</sub>. The presence of aromatic products with two or three nitro substituents also imply that wood tar particles can act as a reservoir or sink for reactive nitrogen oxides (NO<sub>y</sub>). Although these organonitrate and nitro-aromatic compounds have a short lifetime in the atmosphere (a few hours up to a day) due to hydrolysis and photolysis by solar radiation,<sup>66</sup> their influence on regional climate and air pollution (e.g., haze and fog formation) cannot be ignored.<sup>67</sup>

The significant enhancement in the absorption of BB-BrC following night-time NO<sub>3</sub> reactions may affect the impact of biomass burning aerosols and plumes on atmospheric chemistry, climate, and human health. These effects may include changes in the radiative forcing of BB-BrC, changes in atmospheric stability due to absorption at different altitude ranges,<sup>68,69</sup> changes in atmospheric photochemistry (e.g., OH radical production rates,  $O_3$  balance, and reactive nitrogen speciation) due to alterations in UV actinic flux,<sup>66,70,71</sup> and an increasing number of changes in the mutagenic and toxicological effects of BBOA, because of favorable nitration reactions.<sup>72</sup> While this laboratory investigation has not quantified these effects individually, it has demonstrated that a full accounting of the life cycle of BBOA, including night-time reactions and sunlight-driven photochemical bleaching via complex chemical mechanisms, is required.

The chemical evolution of fire plumes in darkness is poorly understood experimentally and is likely complex. Rapid reactions of NO<sub>3</sub> with biomass burning released gaseous volatile organic compounds (BB-VOCs) and the rapid heterogeneous uptake of both NO<sub>3</sub> and N<sub>2</sub>O<sub>5</sub> occur simultaneously.<sup>20</sup> In cases where the latter is dominant, the processes identified here will be of particular significance. Moreover, the presence of inorganic components and black carbon (BC) in both internal and external mixtures with BB-BrC may add complexity to the aging of BrC. Overall, this study demonstrates the atmospheric significance of heterogeneous NO<sub>3</sub> radical reactions in modifying the absorption and chemical composition of BB-BrC species.

#### ■ ASSOCIATED CONTENT

##### Supporting Information

The Supporting Information is available free of charge at <https://pubs.acs.org/doi/10.1021/acs.est.9b05641>.

Detailed experiments, measurements, data analysis, modeling, and additional assisting results, including 6 tables, 13 figures, and 6 text sections (PDF)

#### ■ AUTHOR INFORMATION

##### Corresponding Author

\*E-mail: [yinon.rudich@weizmann.ac.il](mailto:yinon.rudich@weizmann.ac.il).

##### ORCID

Quanfu He: 0000-0002-3229-8206

Uwe Käfer: 0000-0002-4016-0661

Christian George: 0000-0003-1578-7056

Alexander Laskin: 0000-0002-7836-8417

Yinon Rudich: 0000-0003-3149-0201

##### Author Contributions

<sup>▽</sup>These authors have contributed equally to this work.

##### Notes

The authors declare no competing financial interest.

#### ■ ACKNOWLEDGMENTS

This research was partially supported by research grants from the US–Israel Binational Science Foundation (BSF Grant No. 2016093), the Israeli Ministry of Science (Grant No. 3-14010), the Helmholtz Association, and the Weizmann Institute of Science in the framework of the “aeroHEALTH Helmholtz International Lab”. C.L. acknowledges support from the Planning & Budgeting Committee, Israel (2018/19). Q.F. acknowledges support from the Koshland Foundation and the Center for Planetary Sciences, Weizmann Institute of Science. R.Z. and U.K. acknowledge support from the Helmholtz Zentrum München in the framework of new HICE-Aerosol and Health. A.L. and A.H. acknowledge support from the U.S. National Oceanic and Atmospheric Administration (Award No. NA16OAR4310101). S.S.B. acknowledges support from the NOAA Atmospheric Chemistry, Climate and Carbon Cycle Program.

#### ■ REFERENCES

- (1) Chen, J.; Li, C.; Ristovski, Z.; Milic, A.; Gu, Y.; Islam, M. S.; Wang, S.; Hao, J.; Zhang, H.; He, C.; et al. A review of biomass burning: Emissions and impacts on air quality, health and climate in China. *Sci. Total Environ.* **2017**, *579*, 1000–1034.
- (2) Bowman, D. M.; Balch, J. K.; Artaxo, P.; Bond, W. J.; Carlson, J. M.; Cochrane, M. A.; D’Antonio, C. M.; DeFries, R. S.; Doyle, J. C.; Harrison, S. P.; et al. Fire in the Earth system. *Science* **2009**, *324* (5926), 481–484.
- (3) Williams, A. P.; Abatzoglou, J. T.; Gershunov, A.; Guzman-Morales, J.; Bishop, D. A.; Balch, J. K.; Lettenmaier, D. P. Observed impacts of anthropogenic climate change on wildfire in California. *Earth’s Future* **2019**, *7*, 892–910.
- (4) Bond, T. C.; Bergstrom, R. W. Light absorption by carbonaceous particles: An investigative review. *Aerosol Sci. Technol.* **2006**, *40* (1), 27–67.
- (5) Moise, T.; Flores, J. M.; Rudich, Y. Optical properties of secondary organic aerosols and their changes by chemical processes. *Chem. Rev.* **2015**, *115* (10), 4400–4439.
- (6) Vakkari, V.; Kerminen, V. M.; Beukes, J. P.; Tiitta, P.; van Zyl, P. G.; Josipovic, M.; Venter, A. D.; Jaars, K.; Worsnop, D. R.; Kulmala, M.; Laakso, L. Rapid changes in biomass burning aerosols by atmospheric oxidation. *Geophys. Res. Lett.* **2014**, *41* (7), 2644–2651.

- (7) Sedlacek III, A. J.; Buseck, P. R.; Adachi, K.; Onasch, T. B.; Springston, S. R.; Kleinman, L. Formation and evolution of Tar Balls from Northwestern US wildfires. *Atmos. Chem. Phys.* **2018**, *18* (15), 11289–11301.
- (8) Giroto, G.; China, S.; Bhandari, J.; Gorkowski, K.; Scarnato, B.; Capek, T.; Marinoni, A.; Veghte, D.; Kulkarni, G.; Aiken, A.; Dubey, M.; Mazzoleni, A. C. Fractal-like tar ball aggregates from wildfire smoke. *Environ. Sci. Technol. Lett.* **2018**, *5* (6), 360–365.
- (9) Hand, J. L.; Malm, W. C.; Day, D.; Lee, T.; Carrico, J.; Carrillo, J.; Collett, J.; Laskin, A.; Wang, C.; Cowin, J. P.; Iedema, M. J. Optical, physical and chemical properties of tar balls observed during the Yosemite Aerosol Characterization Study. *J. Geophys. Res.* **2005**, *110* (D21), D21210.
- (10) Li, C.; He, Q.; Schade, J.; Passig, J.; Zimmermann, R.; Meidan, D.; Laskin, A.; Rudich, Y. Dynamic changes of optical and chemical properties of tar ball aerosols by atmospheric photochemical aging. *Atmos. Chem. Phys.* **2019**, *19* (1), 139–163.
- (11) Hoffer, A.; Tóth, A.; Nyirő-Kósa, I.; Pósfai, M.; Gelencsér, A. Light absorption properties of laboratory-generated tar ball particles. *Atmos. Chem. Phys.* **2016**, *16* (1), 239–246.
- (12) Jacobson, M. Z. Investigating cloud absorption effects: Global absorption properties of black carbon, tar balls, and soil dust in clouds and aerosols. *J. Geophys. Res.: Atmos.* **2012**, *117*, D06205.
- (13) Sumlin, B. J.; Pandey, A.; Walker, M. J.; Pattison, R. S.; Williams, B. J.; Chakrabarty, R. K. Atmospheric photooxidation diminishes light absorption by primary Brown Carbon aerosol from biomass burning. *Environ. Sci. Technol. Lett.* **2017**, *4* (12), 540–545.
- (14) Forrister, H.; Liu, J.; Scheuer, E.; Dibb, J.; Ziemba, L.; Thornhill, K. L.; Anderson, B.; Diskin, G.; Perring, A. E.; Schwarz, J. P.; et al. Evolution of brown carbon in wildfire plumes. *Geophys. Res. Lett.* **2015**, *42* (11), 4623–4630.
- (15) Zhong, M.; Jang, M. Dynamic light absorption of biomass-burning organic carbon photochemically aged under natural sunlight. *Atmos. Chem. Phys.* **2014**, *14* (3), 1517–1525.
- (16) Browne, E. C.; Zhang, X.; Franklin, J. P.; Ridley, K. J.; Kirchstetter, T. W.; Wilson, K. R.; Cappa, C. D.; Kroll, J. H. Effect of heterogeneous oxidative aging on light absorption by biomass-burning organic aerosol. *Aerosol Sci. Technol.* **2019**, *53* (6), 663–674.
- (17) Saleh, R.; Hennigan, C.; McMeeking, G.; Chuang, W.; Robinson, E.; Coe, H.; Donahue, N.; Robinson, A. Absorptivity of brown carbon in fresh and photo-chemically aged biomass-burning emissions. *Atmos. Chem. Phys.* **2013**, *13* (15), 7683–7693.
- (18) Bluvshstein, N.; Lin, P.; Flores, J. M.; Segev, L.; Mazar, Y.; Tas, E.; Snider, G.; Weagle, C.; Brown, S. S.; Laskin, A.; Rudich, Y. Broadband optical properties of biomass-burning aerosol and identification of brown carbon chromophores. *J. Geophys. Res.: Atmos.* **2017**, *122*, S441–S456.
- (19) Lin, P.; Bluvshstein, N.; Rudich, Y.; Nizkorodov, S. A.; Laskin, J.; Laskin, A. Molecular chemistry of atmospheric Brown Carbon inferred from a nationwide biomass burning event. *Environ. Sci. Technol.* **2017**, *51* (20), 11561–11570.
- (20) Mohr, C.; Lopez-Hilfiker, F. D.; Zotter, P.; Prévôt, A. S.; Xu, L.; Ng, N. L.; Herndon, S. C.; Williams, L. R.; Franklin, J. P.; Zahniser, M. S.; et al. Contribution of nitrated phenols to wood burning brown carbon light absorption in Detling, United Kingdom during winter time. *Environ. Sci. Technol.* **2013**, *47* (12), 6316–6324.
- (21) Decker, Z.; Zarzana, K.; Coggon, M. M.; Min, K.-E.; Pollack, I.; Ryerson, T. B.; Peischl, J.; Edwards, P.; Dubé, W. P.; Markovic, M. Z.; et al. Nighttime chemical transformation in biomass burning plumes: a box model analysis initialized with aircraft observations. *Environ. Sci. Technol.* **2019**, *53* (5), 2529–2538.
- (22) Brown, S.; Ryerson, T.; Wollny, A.; Brock, C.; Peltier, R.; Sullivan, A.; Weber, R.; Dube, W.; Trainer, M.; Meagher, J. F. Variability in nocturnal nitrogen oxide processing and its role in regional air quality. *Science* **2006**, *311* (5757), 67–70.
- (23) Ng, N. L.; Brown, S. S.; Archibald, A. T.; Atlas, E.; Cohen, R. C.; Crowley, J. N.; Day, D. A.; Donahue, N. M.; Fry, J. L.; Fuchs, H.; et al. Nitrate radicals and biogenic volatile organic compounds: oxidation, mechanisms, and organic aerosol. *Atmos. Chem. Phys.* **2017**, *17* (3), 2103–2162.
- (24) Teich, M.; van Pinxteren, D.; Wang, M.; Kecorius, S.; Wang, Z.; Müller, T.; Močnik, G.; Herrmann, H. Contributions of nitrated aromatic compounds to the light absorption of water-soluble and particulate brown carbon in different atmospheric environments in Germany and China. *Atmos. Chem. Phys.* **2017**, *17* (3), 1653–1672.
- (25) Gross, S.; Bertram, A. K. Products and kinetics of the reactions of an alkane monolayer and a terminal alkene monolayer with NO<sub>3</sub> radicals. *J. Geophys. Res.* **2009**, *114*, D02307.
- (26) Knopf, D. A.; Forrester, S. M.; Slade, J. H. Heterogeneous oxidation kinetics of organic biomass burning aerosol surrogates by O<sub>3</sub>, NO<sub>2</sub>, N<sub>2</sub>O<sub>5</sub>, and NO<sub>3</sub>. *Phys. Chem. Chem. Phys.* **2011**, *13* (47), 21050–21062.
- (27) Liu, C.; Zhang, P.; Wang, Y.; Yang, B.; Shu, J. Heterogeneous reactions of particulate methoxyphenols with NO<sub>3</sub> radicals: Kinetics, products, and mechanisms. *Environ. Sci. Technol.* **2012**, *46* (24), 13262–13269.
- (28) Shetty, N. J.; Pandey, A.; Baker, S.; Hao, W. M.; Chakrabarty, R. K. Measuring light absorption by freshly emitted organic aerosols: optical artifacts in traditional solvent-extraction-based methods. *Atmos. Chem. Phys.* **2019**, *19* (13), 8817–8830.
- (29) Bluvshstein, N.; Flores, J. M.; Segev, L.; Rudich, Y. A new approach for retrieving the UV-vis optical properties of ambient aerosols. *Atmos. Meas. Tech.* **2016**, *9* (8), 3477–3490.
- (30) Wong, J. P.; Tsagkaraki, M.; Tsiodra, I.; Mihalopoulos, N.; Violaki, K.; Kanakidou, M.; Sciare, J.; Nenes, A.; Weber, R. J. Atmospheric evolution of molecular-weight-separated brown carbon from biomass burning. *Atmos. Chem. Phys.* **2019**, *19* (11), 7319–7334.
- (31) Lin, P.; Aiona, P. K.; Li, Y.; Shiraiwa, M.; Laskin, J.; Nizkorodov, S. A.; Laskin, A. Molecular characterization of brown carbon in biomass burning aerosol particles. *Environ. Sci. Technol.* **2016**, *50* (21), 11815–11824.
- (32) Phillips, S. M.; Smith, G. D. Light absorption by charge transfer complexes in brown carbon aerosols. *Environ. Sci. Technol. Lett.* **2014**, *1* (10), 382–386.
- (33) Sengupta, D.; Samburova, V.; Bhattarai, C.; Kirillova, E.; Mazzoleni, L.; Iaukea-Lum, M.; Watts, A.; Moosmüller, H.; Khlystov, A. Light absorption by polar and non-polar aerosol compounds from laboratory biomass combustion. *Atmos. Chem. Phys.* **2018**, *18* (15), 10849–10867.
- (34) Rajput, P.; Sarin, M. Polar and non-polar organic aerosols from large-scale agricultural-waste burning emissions in Northern India: implications to organic mass-to-organic carbon ratio. *Chemosphere* **2014**, *103*, 74–79.
- (35) Sun, J.; Ariya, P. A. Atmospheric organic and bio-aerosols as cloud condensation nuclei (CCN): A review. *Atmos. Environ.* **2006**, *40* (5), 795–820.
- (36) Petters, M. D.; Prenni, A. J.; Kreidenweis, S. M.; DeMott, P. J.; Matsunaga, A.; Lim, Y. B.; Ziemann, P. J. Chemical aging and the hydrophobic-to-hydrophilic conversion of carbonaceous aerosol. *Geophys. Res. Lett.* **2006**, *24*, L24806.
- (37) Tóth, Á.; Hoffer, A.; Pósfai, M.; Ajtai, T.; Kónya, Z.; Blazsó, M.; Czégény, Z.; Kiss, G.; Bozóki, Z.; Gelencsér, A. Chemical characterization of laboratory-generated tar ball particles. *Atmos. Chem. Phys.* **2018**, *18* (14), 10407–10418.
- (38) Pósfai, M.; Gelencsér, A.; Simonics, R.; Arató, K.; Li, J.; Hobbs, P. V.; Buseck, P. R. Atmospheric tar balls: Particles from biomass and biofuel burning. *J. Geophys. Res.: Atmos.* **2004**, *109*, D06213.
- (39) Laskin, A.; Smith, J. S.; Laskin, J. Molecular characterization of nitrogen-containing organic compounds in biomass burning aerosols using high-resolution mass spectrometry. *Environ. Sci. Technol.* **2009**, *43* (10), 3764–3771.
- (40) Cubison, M.; Ortega, A.; Hayes, P.; Farmer, D.; Day, D.; Lechner, M.; Brune, W.; Apel, E.; Diskin, G.; Fisher, J.; et al. Effects of aging on organic aerosol from open biomass burning smoke in aircraft and laboratory studies. *Atmos. Chem. Phys.* **2011**, *11* (23), 12049–12064.

- (41) Ng, N.; Canagaratna, M.; Zhang, Q.; Jimenez, J.; Tian, J.; Ulbrich, I.; Kröll, J.; Docherty, K.; Chhabra, P.; Bahreini, R.; et al. Organic aerosol components observed in Northern Hemispheric datasets from Aerosol Mass Spectrometry. *Atmos. Chem. Phys.* **2010**, *10* (10), 4625–4641.
- (42) Li, Y. J.; Yeung, J. W.; Leung, T. P.; Lau, A. P.; Chan, C. K. Characterization of organic particles from incense burning using an aerodyne high-resolution time-of-flight aerosol mass spectrometer. *Aerosol Sci. Technol.* **2012**, *46* (6), 654–665.
- (43) Herring, C. L.; Faiola, C. L.; Massoli, P.; Sueper, D.; Erickson, M. H.; McDonald, J. D.; Simpson, C. D.; Yost, M. G.; Jobson, B. T.; VanReken, T. M. New methodology for quantifying polycyclic aromatic hydrocarbons (PAHs) using high-resolution aerosol mass spectrometry. *Aerosol Sci. Technol.* **2015**, *49* (11), 1131–1148.
- (44) Simoneit, B. R. Biomass burning—a review of organic tracers for smoke from incomplete combustion. *Appl. Geochem.* **2002**, *17* (3), 129–162.
- (45) Christian, T. J.; Kleiss, B.; Yokelson, R. J.; Holzinger, R.; Crutzen, P.; Hao, W. M.; Saharjo, B.; Ward, D. E. Comprehensive laboratory measurements of biomass-burning emissions: 1. Emissions from Indonesian, African, and other fuels. *J. Geophys. Res.* **2003**, *108* (D23), DOI: 10.1029/2003JD003704.
- (46) Shepherd, R. H.; King, M. D.; Marks, A. A.; Brough, N.; Ward, A. D. Determination of the refractive index of insoluble organic extracts from atmospheric aerosol over the visible wavelength range using optical tweezers. *Atmos. Chem. Phys.* **2018**, *18* (8), 5235–5252.
- (47) Washenfelder, R.; Attwood, A.; Brock, C.; Guo, H.; Xu, L.; Weber, R.; Ng, N.; Allen, H.; Ayres, B.; Baumann, K.; et al. Biomass burning dominates brown carbon absorption in the rural southeastern United States. *Geophys. Res. Lett.* **2015**, *42* (2), 653–664.
- (48) Chakrabarty, R.; Moosmüller, H.; Chen, L.-W.; Lewis, K.; Arnott, W.; Mazzoleni, C.; Dubey, M.; Wold, C.; Hao, W.; Kreidenweis, S. Brown carbon in tar balls from smoldering biomass combustion. *Atmos. Chem. Phys.* **2010**, *10* (13), 6363–6370.
- (49) Chen, Y.; Bond, T. Light absorption by organic carbon from wood combustion. *Atmos. Chem. Phys.* **2010**, *10* (4), 1773–1787.
- (50) Levin, E.; McMeeking, G.; Carrico, C.; Mack, L.; Kreidenweis, S.; Wold, C.; Moosmüller, H.; Arnott, W.; Hao, W.; Collett, J.; Malm, W. C. Biomass burning smoke aerosol properties measured during Fire Laboratory at Missoula Experiments (FLAME). *J. Geophys. Res.* **2010**, *115*, D18210.
- (51) Abel, S. J.; Haywood, J. M.; Highwood, E. J.; Li, J.; Buseck, P. R. Evolution of biomass burning aerosol properties from an agricultural fire in southern Africa. *Geophys. Res. Lett.* **2003**, *30* (15), 1783–1786.
- (52) Zhang, X.; Lin, Y.-H.; Surratt, J. D.; Weber, R. J. Sources, composition and absorption Ångström exponent of light-absorbing organic components in aerosol extracts from the Los Angeles Basin. *Environ. Sci. Technol.* **2013**, *47* (8), 3685–3693.
- (53) Chen, Q.; Ikemori, F.; Nakamura, Y.; Vodicka, P.; Kawamura, K.; Mochida, M. Structural and light-absorption characteristics of complex water-insoluble organic mixtures in urban submicrometer aerosols. *Environ. Sci. Technol.* **2017**, *51* (15), 8293–8303.
- (54) Kwon, D.; Sovers, M. J.; Grassian, V. H.; Kleiber, P. D.; Young, M. A. Optical properties of humic material standards: solution phase and aerosol measurements. *ACS Earth and Space Chem.* **2018**, *2* (11), 1102–1111.
- (55) Dinar, E.; Abo Rizeq, A.; Spindler, C.; Erlick, C.; Kiss, G.; Rudich, Y. The complex refractive index of atmospheric and model humic-like substances (HULIS) retrieved by a cavity ring down aerosol spectrometer (CRD-AS). *Faraday Discuss.* **2008**, *137*, 279–295.
- (56) Bruns, E. A.; Perraud, V. r.; Zelenyuk, A.; Ezell, M. J.; Johnson, S. N.; Yu, Y.; Imre, D.; Finlayson-Pitts, B. J.; Alexander, M. L. Comparison of FTIR and particle mass spectrometry for the measurement of particulate organic nitrates. *Environ. Sci. Technol.* **2010**, *44* (3), 1056–1061.
- (57) Kröll, J. H.; Donahue, N. M.; Jimenez, J. L.; Kessler, S. H.; Canagaratna, M. R.; Wilson, K. R.; Altieri, K. E.; Mazzoleni, L. R.; Wozniak, A. S.; Bluhm, H.; et al. Carbon oxidation state as a metric for describing the chemistry of atmospheric organic aerosol. *Nat. Chem.* **2011**, *3* (2), 133–139.
- (58) Hoffmann, D.; Tilgner, A.; Iinuma, Y.; Herrmann, H. Atmospheric stability of levoglucosan: a detailed laboratory and modeling study. *Environ. Sci. Technol.* **2010**, *44* (2), 694–699.
- (59) Pratap, V.; Bian, Q. J.; Kiran, S. A.; Hopke, P. K.; Pierce, J. R.; Nakao, S. Investigation of levoglucosan decay in wood smoke smog-chamber experiments: The importance of aerosol loading, temperature, and vapor wall losses in interpreting results. *Atmos. Environ.* **2019**, *199*, 224–232.
- (60) Hallquist, M.; Wängberg, I.; Ljungström, E.; Barnes, I.; Becker, K.-H. Aerosol and product yields from NO<sub>3</sub> radical-initiated oxidation of selected monoterpenes. *Environ. Sci. Technol.* **1999**, *33* (4), 553–559.
- (61) Lin, P.; Fleming, L. T.; Nizkorodov, S. A.; Laskin, J.; Laskin, A. Comprehensive molecular characterization of atmospheric Brown Carbon by high resolution mass spectrometry with electrospray and atmospheric pressure photoionization. *Anal. Chem.* **2018**, *90* (21), 12493–12502.
- (62) Docherty, K. S.; Ziemann, P. J. Reaction of oleic acid particles with NO<sub>3</sub> radicals: Products, mechanism, and implications for radical-initiated organic aerosol oxidation. *J. Phys. Chem. A* **2006**, *110* (10), 3567–3577.
- (63) Redmond, H.; Thompson, J. E. Evaluation of a quantitative structure-property relationship (QSPR) for predicting mid-visible refractive index of secondary organic aerosol (SOA). *Phys. Chem. Chem. Phys.* **2011**, *13* (15), 6872–6882.
- (64) Bosque, R.; Sales, J. Polarizabilities of solvents from the chemical composition. *J. Chem. Inf. Comput. Sci.* **2002**, *42* (5), 1154–1163.
- (65) Jacobson, M. Z. Isolating nitrated and aromatic aerosols and nitrated aromatic gases as sources of ultraviolet light absorption. *J. Geophys. Res.* **1999**, *104* (D3), 3527–3542.
- (66) Lee, B. H.; Mohr, C.; Lopez-Hilfiker, F. D.; Lutz, A.; Hallquist, M.; Lee, L.; Romer, P.; Cohen, R. C.; Iyer, S.; Kurtén, T.; et al. Highly functionalized organic nitrates in the southeast United States: Contribution to secondary organic aerosol and reactive nitrogen budgets. *Proc. Natl. Acad. Sci. U. S. A.* **2016**, *113* (6), 1516–1521.
- (67) Desyaterik, Y.; Sun, Y.; Shen, X.; Lee, T.; Wang, X.; Wang, T.; Collett, J. L. Speciation of “brown” carbon in cloud water impacted by agricultural biomass burning in eastern China. *J. Geophys. Res.: Atmos.* **2013**, *118* (13), 7389–7399.
- (68) Li, Z.; Guo, J.; Ding, A.; Liao, H.; Liu, J.; Sun, Y.; Wang, T.; Xue, H.; Zhang, H.; Zhu, B. Aerosol and boundary-layer interactions and impact on air quality. *Natl. Sci. Rev.* **2017**, *4* (6), 810–833.
- (69) Raatikainen, T.; Hyvärinen, A. P.; Hatakka, J.; Panwar, T.; Hooda, R.; Sharma, V.; Lihavainen, H. The effect of boundary layer dynamics on aerosol properties at the Indo-Gangetic plains and at the foothills of the Himalayas. *Atmos. Environ.* **2014**, *89*, 548–555.
- (70) Mok, J.; Krotkov, N. A.; Arola, A.; Torres, O.; Jethva, H.; Andrade, M.; Labow, G.; Eck, T. F.; Li, Z.; Dickerson, R. R.; et al. Impacts of brown carbon from biomass burning on surface UV and ozone photochemistry in the Amazon Basin. *Sci. Rep.* **2016**, *6*, 36940.
- (71) Farmer, D.; Perring, A.; Wooldridge, P.; Blake, D.; Baker, A.; Meinardi, S.; Huey, L.; Tanner, D.; Vargas, O.; Cohen, R. Impact of organic nitrates on urban ozone production. *Atmos. Chem. Phys.* **2011**, *11* (9), 4085–4094.
- (72) Purohit, V.; Basu, A. K. Mutagenicity of nitroaromatic compounds. *Chem. Res. Toxicol.* **2000**, *13* (8), 673–692.

1 **Supporting information**

2 **Formation of Secondary Brown Carbon in Biomass Burning Aerosol Proxies through NO<sub>3</sub>**  
3 **Radical Reactions**

4 Chunlin Li,<sup>†,∇</sup> Quanfu He,<sup>†,∇</sup> Anusha Priyadarshani Silva Hettiyadura,<sup>‡</sup> Uwe Käfer,<sup>§,||</sup> Guy Shmul,<sup>⊥</sup>  
5 Daphne Meidan,<sup>†</sup> Ralf Zimmermann,<sup>§,||</sup> Steven S. Brown,<sup>#,★</sup> Christian George,<sup>◆</sup> Alexander Laskin,<sup>‡</sup>  
6 and Yinon Rudich<sup>\*,†</sup>

7 <sup>†</sup>Department of Earth and Planetary Sciences, Weizmann Institute of Science, Rehovot 76100, Israel

8 <sup>‡</sup>Department of Chemistry, Purdue University, West Lafayette, Indiana 47907, United States

9 <sup>§</sup>Joint Mass Spectrometry Centre, University of Rostock, Dr.-Lorenz-Weg 2, 18059 Rostock, Germany

10 <sup>||</sup>Joint Mass Spectrometry Centre, Cooperation Group “Comprehensive Molecular Analytics” (CMA), Helmholtz  
11 Zentrum München, Ingolstadter Landstrasse 1, 85764 Neuherberg, Germany”

12 <sup>⊥</sup>Department of Chemical Research Support, Weizmann Institute of Science, Rehovot 76100, Israel

13 <sup>#</sup>Chemical Science Division, NOAA Earth System Research Laboratory (ESRL), Boulder, Colorado 80305, United States

14 <sup>★</sup>Department of Chemistry, University of Colorado, Boulder, Colorado 80309-0215, United States

15 <sup>◆</sup>Univ Lyon, Université Claude Bernard Lyon 1, CNRS, IRCELYON, F-69626, Villeurbanne, France

16 <sup>∇</sup>Contributed equally

17 <sup>\*</sup>Email: yinon.rudich@weizmann.ac.il

18 **Supporting Information consists of 31 pages, including 13 figures, 6 tables and 6 text sections.**

19	<b>Content:</b>	
20	<b>S1. Wood tar aerosol generation.</b>	<b>3</b>
21	<b>S2. Aerosol flow tube reactor (AFR).</b>	<b>3</b>
22	<b>S3. Generation of NO<sub>3</sub> radicals and NO<sub>3</sub>-N<sub>2</sub>O<sub>5</sub> detection.</b>	<b>3</b>
23	<b>S4. Broadband complex refractive index retrieval.</b>	<b>5</b>
24	<b>S5. Wood tar aerosol chemical composition measurements.</b>	<b>6</b>
25	S5.1. HR-ToF-AMS	<b>6</b>
26	S5.2. Individual particle analysis	<b>7</b>
27	S5.3. Vibrational spectroscopy measurements.	<b>7</b>
28	S5.4. GC×GC/EI-HR-ToF-MS.	<b>7</b>
29	S5.5. (-) ESI-Q-ToF-MS.	<b>7</b>
30	S5.6. HPLC-PDA-(-)ESI/HRMS analysis.	<b>8</b>
31	<b>S6. Chemical box model simulation</b>	<b>13</b>
32	S6.1. NO <sub>3</sub> radical and N <sub>2</sub> O <sub>5</sub> aerosol loss in the AFR (Figure S3-4, Table S2-3).	<b>13</b>
33	S6.2. Quantification of nighttime smoke particle NO <sub>3</sub> aging (Table S4).	<b>13</b>
34	<b>Figures and Tables</b>	
35	Figure S1. Individual particle analysis (ESEM-EDX)	<b>10</b>
36	Figure S2. Chemical results from GC×GC/EI-HR-ToF-MS measurement	<b>11</b>
37	Table S1. Summarized optical results for wood tar particles before and after NO <sub>3</sub> radical reactions	<b>12</b>
38	Table S5. Summarized HR-ToF-AMS results for fresh and NO <sub>3</sub> oxidized wood tar aerosols	<b>19</b>
39	Figure S5. Detailed HR-ToF-AMS spectral changes for wood tar aerosol via NO <sub>3</sub> radical reactions(Nonpolar)	<b>20</b>
40	Figure S6. Detailed HR-ToF-AMS spectral changes for wood tar aerosol via NO <sub>3</sub> radical reactions(Moderately polar)	<b>21</b>
41	Figure S7. Detailed HR-ToF-AMS spectral changes for wood tar aerosol via NO <sub>3</sub> radical reactions(Polar)	<b>22</b>
42	Figure S8. FT-IR results for moderately polar wood tar aerosol in NO <sub>3</sub> radical chemistry	<b>23</b>
43	Figure S9. (-)ESI-Q-ToF-MS spectra for fresh and NO <sub>3</sub> radical reacted wood tar aerosol	<b>24</b>
44	Figure S10. Comparison of elemental features for fresh and NO <sub>3</sub> radical reacted wood tar aerosol	<b>25</b>
45	Table S6. Intensity weighted average molecular characteristics for fresh and NO <sub>3</sub> radical reacted wood tar aerosol	<b>26</b>
46	Figure S11. Proposed reaction pathways in NO <sub>3</sub> radical chemistry with wood tar compounds	<b>26</b>
47	Figure S12. Size resolved chemical composition and mass fraction of NO <sub>3</sub> radical reacted wood tar aerosols	<b>27</b>
48	Figure S13. Detailed broadband RI values as functions of wavelength and NO <sub>3</sub> radical reactions for wood tar aerosol	<b>28</b>

50 **S1. Wood Tar Aerosol Generation.** Detailed procedures for generation of wood tar aerosol can be found elsewhere.<sup>1,2</sup> In short, 100  
51 g commercial wood pellets (Hallingdal Trepellets, water content 7-8 wt.%, 2-3 cm in length, 8 mm in diameter) were smashed, and dry  
52 distilled at 550 °C in a flask combustor equipped with electric heating plate and with controlled high-purity N<sub>2</sub> supply of 1.5 L min<sup>-1</sup>.  
53 Wood tar material in the pyrolysis emissions was collected using a water-cooled condensation system (15 °C for cycling water). The  
54 collected viscous wood tar materials were concentrated by heating to 300 °C under high-purity N<sub>2</sub> atmosphere. The concentrated tar  
55 solution was extracted using ultrapure MiliQ water (18.2 MΩ, UV sterilized), acetonitrile, and a mixture of dichloromethane/hexane  
56 (1:1, v/v). All the extracted samples passed through syringe filters with 0.2 μm Teflon membrane (Pall Life Science) to filter impurities  
57 and particulates. The dichloromethane/hexane extract fractions were dried via rotatory evaporation (water bath at 50 °C) and re-dissolved  
58 in a mixture of acetonitrile and methanol (1:1, v/v). The extracts obtained with the solvents of water, acetonitrile, and organo-mixture of  
59 dichloromethane/hexane are hereafter referred to as polar, moderately polar, and nonpolar wood tar, respectively. All the solvents (e.g.,  
60 acetonitrile, methanol, dichloromethane, and hexane) were used as received with HPLC grade and purity ≥99.9% (Sigma-Aldrich).

61 Following extraction, a constant output atomizer (Model 3076, TSI) was used to nebulize the wood tar solutions with high-purity N<sub>2</sub>  
62 at 15-20 psi pressure. A splitter delivered 0.8 L min<sup>-1</sup> of the aerosols to a quartz heating tube (*L*:20 cm, *ID*: 0.7 cm, maintained at 300 °C,  
63 residence time ~0.6 s), through which wood tar aerosols were dehydrated and compacted, mimicking heat shock in the fire for burning  
64 released particles. Two activated charcoal and one silica gel denuders (*L*:70 cm, *ID*: 7 cm) in series were fixed downstream, for removing  
65 the solvents in both gas and particulate phases. With this procedure, we generated wood tar particles with different chemical polarities.

66 **S2. Aerosol Flow Tube Reactor (AFR).** The flow reactor was a cylindrical glass tube of 7.5 cm inner diameter and length of 72  
67 cm. The input port of the reactor was a conical mixing section fitted with three separated inlets, of which one inlet was connected  
68 downstream of the atomizer system for introduction of the particles, the other two inlets were used to supply O<sub>2</sub> and N<sub>2</sub>O<sub>5</sub>. Prior to  
69 experiments, the flow tube was cleaned with N<sub>2</sub> and high concentration of O<sub>3</sub> until no particles were detected using a condensation  
70 particle counter (CPC, Model 3775 low, TSI). During the experiments, a stable flow of the conditioned wood tar particles at 0.8 L min<sup>-1</sup>  
71 was introduced into the AFR and mixed with 0.2 L min<sup>-1</sup> oxygen (purity of 99.999%). A flow of gaseous N<sub>2</sub>O<sub>5</sub> with N<sub>2</sub> as carrier gas at  
72 0.06-0.10 L min<sup>-1</sup> was added as a source of NO<sub>3</sub> radicals (N<sub>2</sub>O<sub>5</sub> ↔ NO<sub>2</sub> + NO<sub>3</sub>) to oxidize wood tar particles in the presence of NO<sub>2</sub> and  
73 O<sub>2</sub> at room temperature (296.5 ± 0.5 K) in the dark. A laminar flow (Reynolds number < 23.5) of total 1.0-1.1 L min<sup>-1</sup> with a residence  
74 time (RT) of approximately 165 s was achieved in the AFR. Three more charcoal denuders (*L*:70 cm, *ID*: 7 cm) in series were fixed  
75 downstream the flow reactor to adsorb the extra NO<sub>x</sub> and gases that evaporated from the particles before the wood tar aerosols were  
76 characterized. A final N<sub>2</sub> flow of 1.0-1.5 L min<sup>-1</sup> was supplied to dilute the particles flow. To minimize loss of particles and gases in  
77 experiments, conductive rubber tubing was used for the aerosol flow, Teflon tubes and Teflon-made connectors were used to introduce  
78 and carry gases.

79 **S3. Generation of NO<sub>3</sub> Radicals and NO<sub>3</sub>-N<sub>2</sub>O<sub>5</sub> Detection.** Dry N<sub>2</sub>O<sub>5</sub> crystals were prepared as NO<sub>3</sub> radical reservoir prior to  
80 the experiments. Briefly, a flow of NO (≥99.9 %, Verdichtetes Gas) is mixed with ultrahigh purity O<sub>2</sub> (≥99.999%, Air Liquid UK Limited.)  
81 in a glass bulb to produce NO<sub>2</sub>. The NO<sub>2</sub> reacts with O<sub>3</sub> in a Teflon tube connected to a glass bulb. Ozone is generated online with an  
82 ozone generator (Pacific Ozone Tech, USA). The produced N<sub>2</sub>O<sub>5</sub> is trapped as white solid flakes in a glass cryotrap which is kept in a  
83 mixture of ethanol and dry ice (approximately at -72 °C, cold enough to trap N<sub>2</sub>O<sub>5</sub> but not O<sub>3</sub> or NO<sub>2</sub>). The reactions taking place are:





88 In the experiments, gaseous  $\text{N}_2\text{O}_5$  was eluted gently from the cold-trap by a small ultrapure  $\text{N}_2$  flow followed by mixing with  
 89 predefined aerosol flow ( $1.0\text{-}1.1 \text{ L min}^{-1}$ ) in the AFR.  $\text{NO}_3$  radicals from  $\text{N}_2\text{O}_5$  thermal decomposition initiated heterogeneous reactions  
 90 with the particles. Only Teflon tubes and connectors were used to carry  $\text{N}_2\text{O}_5$  before mixing with particles. The  $\text{NO}_3$  radical oxidation  
 91 degrees of wood tar particles depend on initial the  $\text{N}_2\text{O}_5$  mixing ratios which were mediated by controlling the  $\text{N}_2$  flow through the cold-  
 92 trap (60, 80, and 100 sccm, respectively).

93  $\text{N}_2\text{O}_5$  was detected following thermal dissociation by a cavity ring-down spectrometer (CRDS) which has been developed in our  
 94 group.<sup>3-5</sup> Application of CRDS for  $\text{NO}_3$  detection has been extensively described.<sup>6</sup> In short, CRDS consists of a single-wavelength laser  
 95 light and an optical cavity, the light is modulated and introduced into the optical cavity, two high-reflectivity concave mirrors are mounted  
 96 at both ends of the cavity to form a stable optical resonator. The light in the cavity bounces back and forth, the decay time of light  
 97 intensity changes due to gases or/and particles absorption and scattering. The extinction coefficient ( $\alpha_{\text{ext}}$ ) can be directly measured from  
 98 the light decay time for empty cavity ( $\tau_0$ ) and gases or/ and particle filled cavity ( $\tau$ ), as given in Equation S5:

99 
$$\alpha_{\text{ext}} = \frac{L}{lc} \left( \frac{1}{\tau} - \frac{1}{\tau_0} \right)$$
 S5

100 where  $L$  is the optical length, and  $l$  is effective cavity length,  $c$  is light velocity ( $2.998 \times 10^8 \text{ m s}^{-1}$ ). With the known absorption cross  
 101 section ( $\sigma_{\text{abs}}$ ) for the specific gas dispersed across the cavity, its concentration ( $C$ ) can be calculated based on Equation S6:

102 
$$C = \frac{\alpha_{\text{ext}}}{\sigma_{\text{abs-NO}_3}}$$
 S6

103  $\text{N}_2\text{O}_5$  is measured as  $\text{NO}_3$  radical following thermal dissociation at  $85 \text{ }^\circ\text{C}$ , at the  $\text{NO}_3$  radical characteristic absorption at  $662 \text{ nm}$  ( $\sigma_{\text{abs-}}$   
 104  $\text{NO}_3 = (2.23 \pm 0.35) \times 10^{-17} \text{ cm}^2 \text{ molec}^{-1}$ ).<sup>6</sup> The CRDS is equipped with this single-wavelength laser light (HL6545MG, Thorlabs Inc., NJ,  
 105 USA) with output power of approximately 150 mW. Light decay is measured by a photomultiplier tube (PMT, H10721-20, Hamamatsu  
 106 Photonics K.K., Hamamatsu, Japan) at a rate of 10-100 MHz. The cavity consists of a temperature-controlled Teflon-made tube (Length:  
 107 0.979 m, ID: 0.8 cm) which is kept at  $85 \text{ }^\circ\text{C}$  to avoid wall loss of  $\text{NO}_3$  radicals and also to promote thermal composition of  $\text{N}_2\text{O}_5$ . The  
 108 CRDS has a detection limit of  $\sim 0.2 \text{ pptv}$  ( $2\sigma$ ) with integration time of 60 s.

109 The ring-down constant time in the absence of  $\text{NO}_3$  radical was measured by titrating  $\text{NO}_3$  radical with  $\text{NO}$ :



111 Titration reaction of  $\text{NO}_3$  radical occurred in a long Teflon tube (L: 3.0 m, ID: 6.0 mm) upstream of the CRDS. The Teflon tube and  
 112 the CRDS cavity were maintained at  $85 \text{ }^\circ\text{C}$ . Titration reaction in the long Teflon tube lasted approximately 15 s, which was long enough  
 113 to reach equilibrium. At fixed  $\text{N}_2\text{O}_5$  flow (60-100 sccm), the mixing ratio of  $\text{NO}$  was increased slowly until the residual  $\text{NO}_3$  radical  
 114 concentration was less than 10 times of the detection limit from the CRDS measurement. Based on  $\text{NO}$  concentration and dilution ratio,  
 115 the  $\text{N}_2\text{O}_5$  concentration could be calculated. Note that this refers to the  $\text{N}_2\text{O}_5$  concentration from the cold-trap, considering dilution. The  
 116 initial gaseous  $\text{N}_2\text{O}_5$  mixing ratios in the AFR were  $455.1 \pm 100.6$ ,  $635.7 \pm 140.6$ , and  $803.6 \pm 177.7 \text{ ppbv}$ , corresponding to 60, 80, 100  
 117 sccm eluting flow, respectively.

118 **S4. Broadband Complex Refractive Index Retrieval.** The processed wood tar particles were first size-selected using an  
 119 aerodynamic aerosol classifier (AAC, Cambustion, UK). The aerodynamic monodispersed tar particles ( $D_{aero}$ ) were then scanned by a  
 120 scanning mobility particle sizer (SMPS, classifier Model 3080, DMA Model 3081, CPC Model 3775 low, TSI) to get their median  
 121 mobility diameter ( $D_m$ ). Assuming homogeneous chemical nature and spherical shape for wood tar aerosol (verified via electron  
 122 microscopy), the particulate effective density ( $\rho$ ) was calculated by Equation S8:

$$123 \quad \rho = \frac{D_{aero}}{D_m} \times \rho_0 \quad \text{S 8}$$

124 where  $\rho_0$  is unit density of 1.0 g cm<sup>-3</sup>.

125 Based on the known effective density, wood tar particles in mobility size range of 175-375 nm with a step of 25 nm were size-selected  
 126 via AAC in sequence. The size-specific particles were introduced into the dual-channel broadband cavity enhanced spectrometer  
 127 (BBCES) for light extinction ( $\alpha_{ext}$ ) measurements in the wavelength of 315-355 and 380-650 nm (at a resolution of 0.5 nm). Particles  
 128 were size-selected using AAC rather than DMA to avoid the influence of multiply charged particles.<sup>7,8</sup> The  $\alpha_{ext}$  of monodisperse particles  
 129 is determined as the difference in light intensity between a filled cavity and particle-free cavity, taking into account the mirror reflectivity  
 130 and the Rayleigh scattering of the carrier gas (zero air).<sup>9,10</sup> Setup and operation of the BBCES have been described in He et al.<sup>3</sup> Only a  
 131 brief description was mentioned here.

132 A broadband laser-driven white-light lamp (EQ-99CAL LDLS, Energetiq Tech., Inc., MA) equipped with air-cooling and water-  
 133 circulation cooling system is the light source. The light from the lamp ranges from 170 to 2100 nm and is coupled to a multimode optical  
 134 quartz fiber of 1mm core (Energetiq). The deep UV region of the light ( $\lambda < 294$  nm) is removed through a long-pass filter (10CGA-295,  
 135 Newport Corp., CA). A dichroic beamsplitter (400 nm, Dichroic long pass filter, Edmund Optics Inc., NJ) is employed to reflect 315-  
 136 365 nm light into the first optical cavity (BBCES<sub>UV</sub>). Light with wavelength longer than 380 nm is optically filtrated using bandpass  
 137 filters (FineNine Optic Technologies, Inc., CA) and reflected into the second cavity (BBCES<sub>vis</sub>). The coupled light is collimated through  
 138 the dual channels. Each cavity consists of two 2.5 cm, 1 m radius curvature mirrors (FiveNine Optics, USA). The high light reflectivity  
 139 of the mirrors ensures minor loss varies from 90 to 500 ppm within the wavelength range of 380-650nm. After exiting the cavity, the  
 140 light is directly collected using a 0.1 cm F/2 fiber collimator (74-UV, Ocean Optics, Dunedin, FL, USA) into one lead of a two-way  
 141 100 $\mu$ m core HOH-UV-VIS bundle fiber (SROPT-8015, Andor Technology, Belfast, UK) that is linearly aligned along the input slit of  
 142 the grating spectrometer. The spectra are acquired using a 163 mm focal length Czerny-Turner spectrometer (Shamrock SR-163, Andor  
 143 Technology, Belfast, UK) with a charge coupled device (CCD) detector (DU920P-BU, Andor Technology, Belfast, UK) maintained at -  
 144 50 °C. The spectrometer is temperature-controlled at 22.0 $\pm$ 0.1 °C. Dark spectra are acquired with the input shutter (SR1-SHT-9003,  
 145 Andor Technology, Belfast, UK) closed prior to each set of spectra. The wavelength is calibrated using a Hg/Ar pen-ray lamp.

146 The general expression that relates the extinction coefficient ( $\alpha_{ext}$ , in cm<sup>-1</sup>) of sample particles in an N<sub>2</sub> or air-filled cavity, to the  
 147 change in intensity of the transmitted light is given in Equation S9:

$$148 \quad \alpha_{ext}(\lambda, D_m, RI) = R_L \left( \frac{1 - R(\lambda)}{d} + \alpha_{Rayleigh}(\lambda) \right) \left( \frac{I_0(\lambda) - I(\lambda)}{I(\lambda)} \right) \quad \text{S 9}$$

149 Where  $R_L$  is the ratio of the total length to the filled length of the cavity,  $R(\lambda)$  is the mirror reflectivity,  $\alpha_{Rayleigh}(\lambda)$  is the extinction  
 150 coefficient due to Rayleigh scattering by N<sub>2</sub> or air,  $I_0(\lambda)$  is the spectrum (i.e., the wavelength-dependent intensity transmitted through the  
 151 cavity and detected by the CCD) of N<sub>2</sub> or air,  $I(\lambda)$  is the spectrum with particles and gases present.

152 Mirror reflectivity of  $R(\lambda)$  can be calculated using reference pure gases (e.g., N<sub>2</sub>, He, CO<sub>2</sub>) with known wavelength-dependent  
 153 extinction coefficients, taking N<sub>2</sub> and He as reference gases, in Equation S10:

$$154 \quad \frac{1-R(\lambda)}{d} = \frac{I_{N_2}(\lambda) \times \alpha_{\text{Rayleigh-N}_2}(\lambda) - I_{\text{He}}(\lambda) \times \alpha_{\text{Rayleigh-He}}(\lambda)}{I_{\text{He}}(\lambda) - I_{N_2}(\lambda)} \quad \text{S10}$$

155 Together with the  $\alpha_{\text{ext}}$  measurement, number concentration of these size-specific particles was monitored with a condensation particle  
 156 counter (CPC, Model 3775 low, TSI) in parallel with BBCES. Thus, the size-specific particle extinction cross section ( $\sigma_{\text{ext}}$ ) can be  
 157 calculated by Equation S11:

$$158 \quad \sigma_{\text{ext}}(\lambda, D_m, RI) = \frac{\alpha_{\text{ext}}(\lambda, D_m, RI)}{N_p} \quad \text{S11}$$

159 where  $\lambda$  is the incident light wavelength (nm).

160 For spherical and homogeneous particles, RI at each wavelength can be retrieved by minimizing the expression in Equation S12:

$$161 \quad \chi^2(\lambda) = \sum_{i=1}^{N_{Dm}} \left( \frac{\sigma_{\text{ext,measured}}(\lambda) - \sigma_{\text{ext,calculated}}(\lambda)}{\sigma_{\text{ext,measured}}(\lambda)} \right)^2 \quad \text{S12}$$

162 Where  $N_{Dm}$  is the number of diameters measured and  $\sigma_{\text{ext,measured}}$  is the theoretical optical cross section calculated based on Mie-Lorenz  
 163 scattering theory by varying the real and imaginary parts ( $n$  and  $k$ ) of the complex RI. The wood tar particles were size-selected by the  
 164 AAC based on the aerodynamic motion without charging, hence it avoids the contribution of multiply charged particles, generating  
 165 highly monodisperse particles and reducing the errors associated with multiply charged large particles.<sup>7,8</sup>

166 A single-wavelength photoacoustic-cavity ring down spectrometer (PAS-CRDS) was used to directly measure both absorption  
 167 coefficient ( $\alpha_{\text{abs}}$ ) and extinction coefficient ( $\alpha_{\text{ext}}$ ) at  $\lambda=404\text{nm}$ . A diode laser (110 mW, iPulse, Topica Photonics, Munich, Germany) was  
 168 used as light source, and the laser beam was split into two separate optical paths entering into the multi-pass PAS cell and cavity. In the  
 169 PAS, modulated laser light is absorbed by gases or/and particles, generating a modulated acoustic wave whose intensity is proportional  
 170 to the energy absorbed by the sample. The acoustic wave is recorded by a sensitive microphone, which has a characteristic radial and  
 171 longitudinal resonance when the light source is modulated at the cavity resonance frequency. The specific resonance frequency of the  
 172 system is found by producing white noise using a speaker in the reference resonator. The PAS calibration procedure is described in our  
 173 previous work.<sup>9</sup> In short, we used standard particulate nigrosin dye with defined RIs, size, and concentration to construct an operational  
 174 function between dry particle absorption coefficients and PAS signals. The RI retrieval method is the same as Equation S12. The  
 175 retrievals have been validated by measuring standard samples and materials, e.g., ammonium sulfate ((NH<sub>4</sub>)<sub>2</sub>SO<sub>4</sub>), polystyrene latex  
 176 (PSL), soot, humic-like substance (HULIS), etc, referring to our previous work.<sup>4,11-13</sup>

177 **S5. Wood Tar Aerosol Chemical Composition Measurements.** The fresh and NO<sub>3</sub> radical processed wood tar aerosols were  
 178 characterized in chemical transformation via both *in situ* and offline techniques.

179 **S5.1. HR-ToF-AMS** was applied to monitor the bulk non-refractive composition of wood tar particles online. The mass spectra were  
 180 acquired in both the high-sensitivity V- and high-resolution W-modes. The vaporizer temperature was set at about 600 °C, and electron-  
 181 ionization energy was 70 eV. The data was analyzed using the Squirrel v 1.16A and PIKA v 1.57 codes ([http://cires.colorado.edu/jimenez-](http://cires.colorado.edu/jimenez-group/ToFAMSResources/ToFSoftware/)  
 182 [group/ToFAMSResources/ToFSoftware/](http://cires.colorado.edu/jimenez-group/ToFAMSResources/ToFSoftware/)). All the organic ions were classified into five groups as C<sub>x</sub>H<sub>y</sub> (including C<sub>x</sub>), C<sub>x</sub>H<sub>y</sub>O, C<sub>x</sub>H<sub>y</sub>O<sub>z</sub>  
 183 (H<sub>x</sub>O<sub>y</sub>, CO, and CO<sub>2</sub> included), C<sub>x</sub>H<sub>y</sub>O<sub>i</sub>N<sub>p</sub>, and NO<sub>y</sub> based on their elemental compositions, where x, y, p ≥ 1, i ≥ 0, and z ≥ 2. Mass spectrum  
 184 was processed from V-mode results, and elemental analyses to determine the molar elemental ratios (C/O, H/O, and N/O) and mass ratio

185 of organic matter to organic carbon (OM/OC) were based on W-mode results.<sup>14</sup>

186 **S5.2. Individual particle analysis.** The particles collected on polycarbonate membranes were imaged using a Quattro Environmental  
187 scanning electron microscopes (ESEM, ThermoScientific Quattro S), and semi-quantitative elemental compositions (O, C, N, and S) of  
188 these particles were acquired from the energy-dispersive X-ray analysis (EDX).

189 **S5.3. Vibrational spectroscopy measurements.** The characteristic functional groups of wood tar aerosols were measured using an FT-  
190 IR (Thermo Scientific Nicolet™ 6700). To moderately polar and nonpolar wood tar samples, Teflon filter loaded samples were extracted  
191 using a mixture of tetrahydrofuran and dichloromethane (1:1, v/v), the extracts were then concentrated using a mild N<sub>2</sub> flush and coated  
192 onto polished KBr windows uniformly (Diameter: 13 mm, Thickness: 2 mm, Spectra-Tech Inc.). The coated windows were further dried  
193 in N<sub>2</sub> purge before being analyzed. To the polar wood tar aerosol, particles were directly impacted onto KBr window. IR spectra for the  
194 samples were recorded over the range of 4000–400 cm<sup>-1</sup> at room temperature using 32 scans at 2 cm<sup>-1</sup> resolution. Ultrapure N<sub>2</sub> flush in  
195 the FT-IR cabinet was applied during spectra recording to avoid environmental CO<sub>2</sub> and moisture influence. The spectrum baseline was  
196 determined by analyzing the blank KBr window and subtracted the blank from the sample spectrum.

197 **S5.4. GC×GC/EI-HR-ToF-MS.** Solvent extracts were prepared by washing each operational blank and sampled Teflon filters in  
198 methanol using vortex shaking (Vortex Genie-2, Scientific Industries) method, the extracts were treated with filtration (0.2 μm PTFE  
199 syringe filter, Pall Life Science) and concentrated via gentle N<sub>2</sub> blowing, ensuring high extraction efficiency, clarity, and high  
200 concentrations of the extracts. Afterward, portions of the extracts were analyzed by a two-dimensional gas chromatography coupled to  
201 electron impact ionization high-resolution multi-reflection time-of-flight mass spectrometry (GC×GC/EI-HR-ToF-MS) to reveal their  
202 molecular composition. The description and operation of this instrument can be found elsewhere.<sup>15,16</sup> In brief, the comprehensive GC×GC  
203 is performed with a first dimension medium-polarity capillary column (59 m×0.25 mm i.d.×0.1 μm, BPX50, SGE Analytical Science,  
204 Ringwood, Australia) and a nonpolar second dimension column (2.4 m×0.10 mm i.d.×0.1 μm, BPX1, SGE Analytical Science, Ringwood,  
205 Australia) to separate organic compounds by their diverse volatility and polarity. After sample injection via programmable temperature  
206 vaporization (50–400°C at 1 °C s<sup>-1</sup>), the GC oven was ramped from initial 50 °C (5 min hold) to 310 °C at 2 °C min<sup>-1</sup> and held for 5 min.  
207 A dual-stage thermal modulator, consisting of a guard nonpolar column (0.1 m×0.10 mm i.d.×0.1 μm, BPX1, SGE Analytical Science,  
208 Ringwood, Australia), was used as the interface between the two columns, where the effluent from the first column was cryogenically  
209 focused and periodically heated for rapid transfer into the second column with modulation period of 5.0 s. The second column was  
210 housed in a secondary oven, which was maintained at 5 °C above the main oven temperature during temperature-rise period. Analytes  
211 were ionized via electron impact ionization (70 eV) and spectra were collected with a high-resolution ( $m/\Delta m > 25,000$ ) multi-reflection  
212 time-of-flight mass spectrometer.

213 **S5.5. (-)ESI-Q-ToF-MS.** Electrospray ionization (ESI) coupled with a quadrupole time-of-flight tandem mass spectrometry (Xevo G2  
214 Q-ToF MS, Waters, Manchester, UK) provided detailed molecular characterization of organic compounds due to its high resolution  
215 ( $m/\Delta m \geq 30,000$ ) and mass accuracy ( $\leq 5$  ppm). ESI is commonly used soft ionization method that minimizes fragmentation of analytes,  
216 allowing for detection of intact molecules. These analytical approaches were applied to characterize the complex mixture of wood tar  
217 materials before and after NO<sub>3</sub> radical oxidation. After optimization, the extracts were directly infused at a flow rate of 10 μL min<sup>-1</sup> and  
218 monitored in negative ESI mode. All spectra were acquired in the mass range 50–2000 m/z. These analyses were performed using a  
219 capillary voltage of 2.50kV, a source temperature of 120°C, a cone voltage of 20V. The desolvation temperature was set to 250°C and  
220 the desolvation gas (N<sub>2</sub>) flow rate was approximately 6 L min<sup>-1</sup>. All measurements were done with Leucine-Enkephalin (200 μg μL<sup>-1</sup>) as

221 a lockspray reference at flow rate of 10  $\mu\text{L min}^{-1}$  to ensure mass accuracy and follow resolution mode. Data acquisition and recording  
 222 were done by Waters MassLynx v4.2 software. The ESI-HRMS data were processed with an open source software toolbox, MZmine 2  
 223 (<http://mzmine.github.io/>), to perform signal deconvolution and peak assignment. Peaks with signal to noise ratio less than 10 and peaks  
 224 appeared in blanks were discarded. Formula assignments were performed using following constraints for the number of atoms in the  
 225 ions:  $2 \leq C \leq 100$ ,  $2 \leq H \leq 200$ ,  $N \leq 3$ ,  $O \leq 50$ ,  $S \leq 1$ , and  $Cl \leq 1$  within 0.001  $\Delta m/z$  tolerance or accuracy  $\leq 5$  ppm. Moreover, some other  
 226 constraints include double-bond equivalent (DBE) to carbon ratio ( $DBE/C \leq 1$ ), elemental ratios ( $0.4 \leq H/C \leq 2.2$ ,  $O/C \leq 1.2$ ,  $N/C \leq 0.5$ ,  
 227  $S/C \leq 0.2$ ), and carbon oxidation state ( $\overline{OS}$ ,  $-3.5 \leq \overline{OS} \leq 3.5$ ) were applied.

228 For an individual compound, DBE and  $\overline{OS}$  of  $C_cH_hO_oN_n$  can be calculated as follows<sup>17,18</sup>:

$$229 \quad DBE = 1 + \frac{n-h}{2} + c \quad S13$$

$$230 \quad \overline{OS} = 2 \times \frac{o}{c} - \frac{h}{c} - 5 \times \frac{n}{c} \quad S14$$

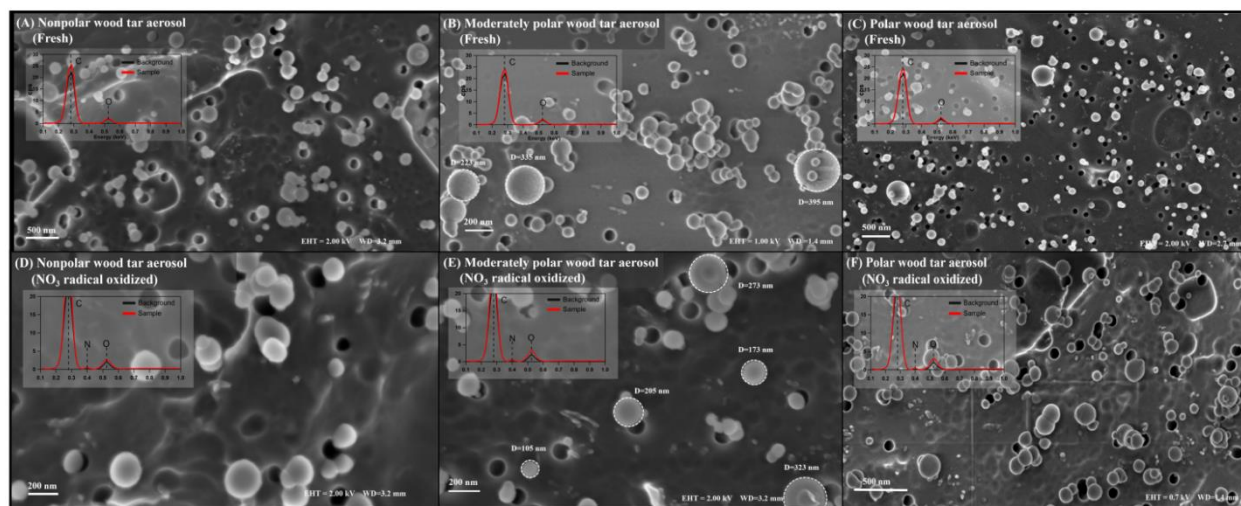
231 Where c, h, o, and n are the atom number for C, H, O, and N, respectively. Both DBE and  $\overline{OS}$  do not consider S condition to the  
 232 chemical formula, and DBE assumes a valence of 3 for nitrogen, therefore, Equation S13 may underestimate the real DBE for nitro-  
 233 compounds (R-NO<sub>2</sub>) and organonitrate (R-ONO<sub>2</sub>).

234 In view of the molecular complexity in bulk materials like wood tar aerosol, hundreds and thousands of compounds may be identified  
 235 from mass spectrum, it is common to express the bulk composition as averaged elemental composition and characteristics (C, H, O, N,  
 236 S, O/C, H/C, N/C, DBE, and  $\overline{OS}$ ) via Equation S15<sup>19</sup>:

$$237 \quad \langle Y \rangle = \frac{\sum_i x_i Y_i}{\sum_i x_i} \quad S15$$

238 Where  $Y_i$  is elemental composition and ratios for  $i_{th}$  molecular formula,  $x_i$  is intensity or peak height of the assigned  $i_{th}$  molecular formula.

239 **S5.6. HPLC-PDA(-)ESI/HRMS analysis.** Unprocessed and NO<sub>3</sub>-reacted wood tar aerosol extracts were also analyzed using a Vanquish  
 240 ultra-high performance liquid chromatographic (HPLC) system coupled with a photodiode array detector (PDA) and an Q Exactive HF-  
 241 X high resolution mass spectrometer (HRMS) equipped with an electrospray ionization (ESI) source (all HPLC-PDA-ESI/HRMS  
 242 modules are from Thermo Scientific, Inc). Samples were separated on a reversed-phase column (Luna C18, 150×2 mm<sup>2</sup>, 5  $\mu\text{m}$  particles,  
 243 100  $\text{\AA}$  pores, Phenomenex, Inc.) using a binary solvent mixture containing LC-MS grade water with 0.1% (v/v) formic acid (A) and LC-  
 244 MS grade acetonitrile with 0.1% (v/v) formic acid (B). A flow rate of 200  $\mu\text{L min}^{-1}$  and a sample injection volume of 5  $\mu\text{L}$  were used.  
 245 The analyte was separated using a stepwise gradient; 0-3 min at 90% of A, 3-90 min a linear gradient to 0% of A, 90-100 min held at 0%  
 246 of A, 100-101 min a linear gradient to 90% of A, and 101-120 min held at 90% of A to re-equilibrate the column at the initial mobile  
 247 phase conditions for the next sample. UV-Vis absorption spectra for the eluted chemicals were measured using the PDA detector over  
 248 the wavelength range of 200-700 nm. We specifically focused on negative mode ESI due to its preference in detecting compounds with  
 249 acidic protons (e.g., nitro-phenols and carboxylic acids).<sup>20,21</sup> The raw data were acquired using Xcalibur software (Thermo Scientific)  
 250 and were processed using Xcalibur software and an online LC-MS data processing software (MZmine-2.38). Formula assignment was  
 251 performed according to the Xcalibur and MIDAS formula calculator. ESI-HRMS in combination with high-performance liquid  
 252 chromatography (HPLC) with a photodiode array (PDA) detector was used to separate BrC compounds based on their retention times  
 253 in conjunction with their light-absorbing properties, thus elucidating their plausible molecular structures. Details refer to the previous  
 254 work.<sup>20,21</sup>



255

256

257

258

259

260

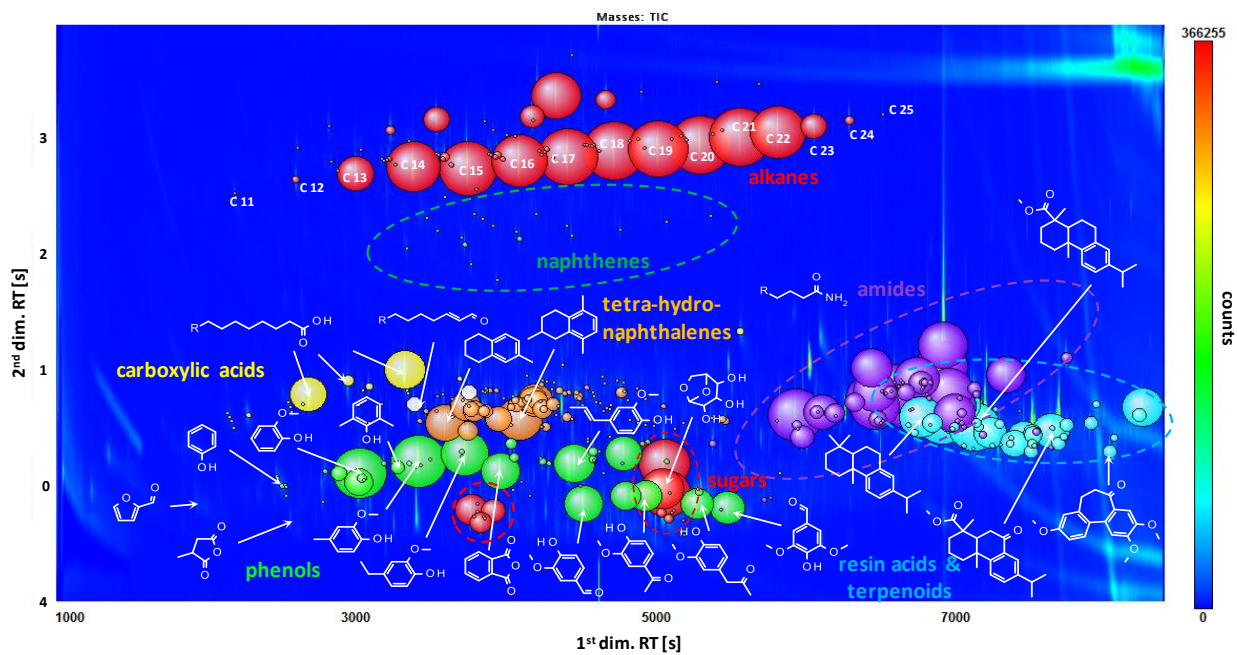
261

262

263

264

**Figure S1.** Individual particle morphology and elemental compositions for (A)-(C) fresh, and (D)-(F) after 13.3 h equivalent ambient  $\text{NO}_3$  radical exposure processed wood tar aerosols. EDX (X-ray energy-disperse spectrometer) spectra averaged from selected particles are shown to indicate the semi-quantitative elemental composition. Wood tar aerosols generated in the laboratory are spherical amorphous carbonaceous particles containing major C and minor O, after exposing to  $\text{NO}_3$  radicals, weak nitrogen additions were detected. The nitrogen signals are probably underestimated due to evaporation or/and decomposition of the nitrogen-bearing organic products in EDX measurements. Semi-quantitative elemental ratios of O/C were calculated as 0.058, 0.108, and 0.345 for fresh nonpolar, moderately polar, and polar wood tar particles, respectively. After  $\text{NO}_3$  radical process, the ratios increased to 0.066, 0.229, 0.478 in accordance with the polarity.



265

266 **Figure S2.** GCxGC/EI-HR-ToF-MS chromatogram of fresh moderately polar wood tar aerosol. Second dimension retention time (RT)

267 is shifted 4 seconds to adjust for wrap around. Exemplary chemical structures of most abundant peaks are shown for identified chemical

268 groups (e.g., phenols, sugars, carboxylic acids, amides, naphthalenes, naphthenes, amides, etc). The circle size indicates relative signal

269 intensity.

**Table S1.** Summarized optical and density results for fresh and NO<sub>3</sub> oxidized wood tar aerosols

Wood tar aerosol	CRDS-PAS @ 404 nm	SSA @ 404 nm	BBCES @ 404 nm	$-\ln(k)/\ln(\lambda)$	AAE	Particle density (g cm <sup>-3</sup> )
Polar wood tar_fresh	(1.536 ± 0.020) + (0.007 ± 0.001)i	0.968	(1.545 ± 0.007) + (0.008 ± 0.003)i	8.103	9.103	1.350 ± 0.015
8.26 ± 2.33 h EAN	(1.533 ± 0.011) + (0.009 ± 0.003)i	0.956	(1.538 ± 0.007) + (0.009 ± 0.003)i	7.863	8.863	1.341 ± 0.014
11.66 ± 2.74 h EAN	(1.524 ± 0.005) + (0.013 ± 0.001)i	0.942	(1.522 ± 0.010) + (0.018 ± 0.006)i	4.739	5.739	1.332 ± 0.016
13.26 ± 3.09 h EAN	(1.520 ± 0.009) + (0.014 ± 0.003)i	0.936	(1.506 ± 0.013) + (0.023 ± 0.005)i	4.103	5.103	1.319 ± 0.015
Moderately polar wood tar_fresh	(1.589 ± 0.004) + (0.018 ± 0.002)i	0.931	(1.584 ± 0.005) + (0.016 ± 0.001)i	8.444	9.444	1.248 ± 0.012
8.26 ± 2.33 h EAN	(1.579 ± 0.002) + (0.022 ± 0.001)i	0.917	(1.570 ± 0.003) + (0.021 ± 0.001)i	6.727	7.727	1.244 ± 0.014
11.66 ± 2.74 h EAN	(1.574 ± 0.003) + (0.024 ± 0.002)i	0.907	(1.553 ± 0.003) + (0.022 ± 0.001)i	5.580	6.580	1.223 ± 0.011
13.26 ± 3.09 h EAN	(1.561 ± 0.006) + (0.028 ± 0.002)i	0.891	(1.534 ± 0.002) + (0.031 ± 0.001)i	4.739	5.739	1.193 ± 0.007
Nonpolar wood tar_fresh	(1.597 ± 0.004) + (0.024 ± 0.001)i	0.915	(1.608 ± 0.002) + (0.023 ± 0.002)i	6.753	7.753	1.194 ± 0.006
8.26 ± 2.33 h EAN	(1.585 ± 0.003) + (0.027 ± 0.003)i	0.901	(1.593 ± 0.003) + (0.026 ± 0.002)i	5.701	6.701	1.182 ± 0.009
11.66 ± 2.74 h EAN	(1.582 ± 0.004) + (0.029 ± 0.002)i	0.892	(1.585 ± 0.004) + (0.032 ± 0.002)i	5.418	6.418	1.182 ± 0.008
13.26 ± 3.09 h EAN	(1.576 ± 0.005) + (0.032 ± 0.003)i	0.884	(1.567 ± 0.005) + (0.036 ± 0.003)i	5.121	6.121	1.181 ± 0.004

Note: CRDS-PAS retrieved RI contains real part from CRDS measurement and imaginary part from PAS measurement. SSA for 250 nm wood tar aerosol was calculated using extinction and absorption cross section values from CRDS-PAS directly measurement at 404 nm. Imaginary  $k$ -derived absorption Angström Exponent (AAE) was regressed over wavelength range of 315–450 nm. For polar wood tar aerosol, AAE was fitted over the measured effective wavelength range of 315–425 nm

## S6. Chemical Box Model Simulations.

**S6.1. NO<sub>3</sub> radical and N<sub>2</sub>O<sub>5</sub> aerosol loss in the AFR.** Heterogeneous reactions occurred when wood tar particles mixed with gaseous N<sub>2</sub>O<sub>5</sub> and NO<sub>3</sub> radicals in the AFR. However, the conversion efficiency of N<sub>2</sub>O<sub>5</sub> to NO<sub>3</sub> at equilibrium depends on the precursor concentration and temperature. At room temperature and initial N<sub>2</sub>O<sub>5</sub> concentration of 500-1000 ppbv, less than 10% of N<sub>2</sub>O<sub>5</sub> will thermally dissociate to produce NO<sub>3</sub> radicals at equilibrium. N<sub>2</sub>O<sub>5</sub> and NO<sub>3</sub> radicals involve different heterogeneous reaction pathways. Through hydrolysis to produce nitric acid is the main reaction of N<sub>2</sub>O<sub>5</sub> on particle surfaces, previous studies confirmed that N<sub>2</sub>O<sub>5</sub> taken by organic surface can be efficient nitrating agent.<sup>22,23</sup> In parallel, NO<sub>3</sub> radicals can initiate a series of oxidation reactions in the presence of NO<sub>2</sub> and O<sub>2</sub>.<sup>24-26</sup> The overall sink of NO<sub>3</sub> radical and N<sub>2</sub>O<sub>5</sub> in the experiment can be simply described by the pseudo-first-order loss to the particle surface and to the wall of the AFR via Equation S16-S18:<sup>27,28</sup>

$$\frac{d[G]}{dt} = -(k_p[G] + k_w[G]) \quad \text{S 16}$$

$$k_p = \frac{\gamma_{eff} \times \omega \times S}{4} = \frac{1}{4} \omega \times S \times \left( \frac{1}{\gamma_p} + \frac{1}{\Gamma_{diff-p}} \right)^{-1} \quad \text{S 17}$$

$$k_w = \frac{\gamma_{eff} \times \omega}{4} \times \frac{S_{AFR}}{V_{AFR}} = \frac{\omega}{D_{int}} \times \left( \frac{1}{\gamma_w} + \frac{1}{\Gamma_{diff-w}} \right)^{-1} \quad \text{S 18}$$

Where  $k_p$  and  $k_w$  represent pseudo-first order loss rate to particle surface and to reactor inner wall, respectively.  $\gamma_{eff}$  is effective uptake coefficient (unitless) for gas  $G$ .  $\omega$  is molecular speed of gas  $G$  ( $\omega$ , m s<sup>-1</sup>).  $S$  is total particle surface area exposed to reactant (cm<sup>2</sup> m<sup>-3</sup>).  $S_{AFR}$  and  $V_{AFR}$  are inner surface area and volume of the reactor.  $D_{int}$  is the inner diameter of the cylindrical flow reactor we used.  $\gamma_p$  and  $\gamma_w$  are uptake coefficient (unitless) to particle surface and to the AFR inner wall.  $\Gamma_{diff}$  describes the gas phase diffusion limitation (unitless) in particle and reactor surface uptake. For the uptake onto monodisperse spherical particles, several methods have been suggested to calculate  $\Gamma_{diff-p}$ .<sup>29,30</sup> The regular method is described as the Fuchs-Sutugin equation in S19:

$$\frac{1}{\Gamma_{diff-p}} = \frac{0.75 + 0.286 \times Kn}{Kn \times (Kn + 1)} \quad \text{S 19}$$

Where  $Kn$  is Knudsen number, given by Equation S20:

$$Kn = \frac{6D}{\omega \times Dp} \quad \text{S 20}$$

The Knudsen number is a function of particle diameter ( $Dp$ , nm), gas-phase diffusion coefficient ( $D$ , torr cm<sup>2</sup> s<sup>-1</sup>) for gaseous molecular  $G$ , and molecular speed  $\omega$ . For fast uptake process (lower  $\Gamma_{diff}$  and higher  $\gamma$ ) and large particles, gas phase diffusion can limit the overall rate of the uptake of  $G$  onto the particle surface. For heterogeneous reactions occurring with polydispersed particles, we can rewrite the above first-order reaction kinetic  $k_{het}$  as Equation S21, taking first-order wall loss of the particles into account:

$$k_p = \frac{1}{4} \omega \times \sum_i \left[ N_i \times \pi \times D_i^2 \times (1 - k_{wall-p} t) \times \left( \frac{1}{\gamma_p} + \frac{1}{\Gamma_{diff-p}} \right)^{-1} \right] \quad \text{S 21}$$

Where  $N_i$  is number concentration (m<sup>-3</sup>) for particle of size  $D_i$  (nm),  $k_{wall-p}$  is first-order wall loss rate (s<sup>-1</sup>) for particles.

In our experiments, we did not observe significant wood tar particle losses to the wall of the AFR based on SMPS and CPC measurements. Thereby, the wall loss rate for wood tar particles can be neglected to get Equation S22:

$$k_p = \frac{1}{4} \omega \times \sum_i \left[ N_i \times \pi \times D_i^2 \times \left( \frac{1}{\gamma_p} + \frac{1}{\Gamma_{diff-p}} \right)^{-1} \right] \quad \text{S 22}$$

$\Gamma_{diff-w}$  is the NO<sub>3</sub> radical and N<sub>2</sub>O<sub>5</sub> wall loss to the AFR, as suggested as Equation S23:

$$\frac{1}{\Gamma_{diff-w}} = \frac{\omega \times D_{int}}{4 \times 3.66 \times D} \quad \text{S 2 3}$$

For the case where the loss rate of gases to the reactor wall is not determined by surface reactivity, but by the diffusion through the gas phase ( $\gamma_w > \Gamma_{wall} \sim 7 \times 10^{-6}$ ), the following expression holds:

$$k_w = \frac{\omega}{D_{int}} \times \left( \frac{1}{\gamma_w} + \frac{1}{\Gamma_{diff-w}} \right)^{-1} \approx \frac{\omega \times \Gamma_{diff-w}}{D_{int}} = \frac{4 \times 3.66 \times D}{D_{int}^2} \quad \text{S 2 4}$$

Equation S24 is valid for Peclet numbers in excess of  $\sim 20$ .<sup>31</sup> This study results in Peclet numbers ( $Pe = D_{int} \times v / D$ , where  $v$  is the average linear velocity of the gas flow) of  $\sim 26$  for NO<sub>3</sub> radical and  $\sim 37$  for N<sub>2</sub>O<sub>5</sub>.

The reactive uptake coefficient ( $\gamma$ ) depends on the reactant and particle surface available.<sup>32,33</sup> Various values have been reported for NO<sub>3</sub> radicals and N<sub>2</sub>O<sub>5</sub> uptake by different chemical surfaces. For NO<sub>3</sub> radical, the uptake coefficients vary considerably from approximately  $2 \times 10^{-4}$  for NO<sub>3</sub> on solid saturated organics up to  $\gamma \geq 0.1$  for some liquid unsaturated organics and phenols.<sup>34,35</sup> Only a few values for biomass burning-related surrogates (e.g., hydrocarbon PAHs, phenols, levoglucosan, etc.) were reported to be in the range of 0.08-0.79 or 0.01-0.03 for NO<sub>3</sub> radicals and less than  $6.6 \times 10^{-5}$  for N<sub>2</sub>O<sub>5</sub> at room temperature and pressure in dry air.<sup>22,23,36</sup> The reported reactive uptake coefficient of NO<sub>3</sub> radicals on methoxy-phenol surface can be  $\sim 3$  orders of magnitude greater than those of NO<sub>2</sub> and N<sub>2</sub>O<sub>5</sub>.<sup>32,35</sup> From our previous work and HR-ToF-AMS/FT-IR results in this study, the wood tar aerosols we generated comprise large fractions of aromatics and phenols, then the uptake coefficient of  $10^{-2}$  and  $10^{-5}$  was applied for NO<sub>3</sub> radical and N<sub>2</sub>O<sub>5</sub>, respectively. According to Tang et al., averaged gas-phase diffusion coefficient of NO<sub>3</sub> is  $92 \pm 46$  torr cm<sup>2</sup> s<sup>-1</sup>, and N<sub>2</sub>O<sub>5</sub> has a diffusion coefficient of  $65 \pm 33$  torr cm<sup>2</sup> s<sup>-1</sup>.<sup>37</sup> Based on number size distributions of wood tar aerosols measure from SMPS (Figure S3), the integrated heterogeneous reaction kinetics at environment condition (1 atm and 296.6 K) were calculated and together with wall loss rates were listed in Table S2:

**Table S2.** Estimated reaction kinetics for NO<sub>3</sub> radicals and N<sub>2</sub>O<sub>5</sub> interaction with wood tar aerosols and reactor inner surface wall

Gas/ Wood tar aerosol	Pseudo-first-order reaction kinetics ( $k_p$ , s <sup>-1</sup> )				Pseudo-first-order wall loss rate ( $k_w$ , s <sup>-1</sup> )
	Nonpolar	Moderately polar	Polar	Average	
NO <sub>3</sub>	$(1.73 \pm 0.21) \times 10^{-2}$	$(1.88 \pm 0.13) \times 10^{-2}$	$(1.85 \pm 0.15) \times 10^{-2}$	$(1.82 \pm 0.21) \times 10^{-2}$	0.031 ± 0.015
N <sub>2</sub> O <sub>5</sub>	$(1.31 \pm 0.16) \times 10^{-5}$	$(1.42 \pm 0.11) \times 10^{-5}$	$(1.39 \pm 0.11) \times 10^{-5}$	$(1.37 \pm 0.15) \times 10^{-5}$	0.022 ± 0.011

Sufficient denuders were used to remove solvents (H<sub>2</sub>O, CH<sub>3</sub>OH, CH<sub>3</sub>CN) from atomized aerosols. Attention should still be paid to the residual gaseous solvents and their competitive reactions with N<sub>2</sub>O<sub>5</sub> and NO<sub>3</sub> radicals in the AFR, due to their high vapor pressure and incomplete filtration through the denuders. The humidity downstream of the AFR in the polar tar aerosol experiment was less than 0.2% (upper limit H<sub>2</sub>O molecule concentration of  $1.536 \times 10^{15}$  molecules cm<sup>-3</sup> in the AFR). We assumed that the solvents were saturated in the gas phase from the atomizer (296.6 ± 0.5 K, 1 atm) and each denuder has 80% filtration efficiency to remove gaseous solvent. The final gaseous CH<sub>3</sub>CN and CH<sub>3</sub>OH entering the flow tube reactor were estimated to be  $7.830 \times 10^{15}$  and  $1.211 \times 10^{16}$  molecules cm<sup>-3</sup> at maximum, respectively.

A simplified model including 10 homogeneous reactions in the gas phase, 4 heterogeneous uptake reactions, and first-order wall loss of N<sub>2</sub>O<sub>5</sub>-NO<sub>3</sub>-NO<sub>2</sub> was developed to estimate the reactive uptake of NO<sub>3</sub> radical and N<sub>2</sub>O<sub>5</sub> by wood tar aerosol in the AFR.<sup>32-38</sup> The

kinetics and reaction pathways applied in model simulation were summarized in Table S3.

**Table S3.** Reaction pathways and rate constants for the modeling of the experiment

Reaction pathways		Reaction rate constant (295K) ( $\text{molec}^{-1} \text{cm}^3 \text{s}^{-1}$ )	Reactive uptake coefficient ( $\gamma$ )	First-order wall loss rate/ heterogeneous reaction kinetics ( $k_{het}, \text{s}^{-1}$ )	Reference or source
Gaseous	$\text{NO}_3 + \text{NO}_2 \rightleftharpoons \text{N}_2\text{O}_5$	$k_{eq(T)} = 2.7 \times 10^{-27} \times e^{11000/T}$			Ayres et al., 2015
Gaseous	$\text{NO}_3 + \text{NO}_2 \rightarrow \text{N}_2\text{O}_5$	$1.66 \times 10^{-12}$			NIST Kinetic
Gaseous	$\text{N}_2\text{O}_5 + \text{H}_2\text{O} \rightarrow 2\text{HNO}_3$	$2.5 \times 10^{-22}$			NIST Kinetic
Gaseous	$\text{NO}_3 + \text{H}_2\text{O} \rightarrow \text{HNO}_3 + \text{OH}$	$2.5 \times 10^{-22}$			NIST Kinetic
Gaseous	$\text{NO}_2 + \text{NO}_3 \rightarrow \text{O}_2 + \text{NO} + \text{NO}_2$	$6.56 \times 10^{-16}$			NIST Kinetic
Gaseous	$\text{NO}_3 + \text{NO}_3 \rightarrow \text{O}_2 + 2\text{NO}_2$	$2.29 \times 10^{-16}$			NIST Kinetic
Gaseous	$\text{CH}_3\text{CN} + \text{NO}_3 \rightarrow \text{CH}_3\text{CN-NO}_3$	$< 5.0 \times 10^{-19}$			NIST Kinetic
Gaseous	$\text{CH}_3\text{CN} + \text{N}_2\text{O}_5 \rightarrow \text{CH}_3\text{CN-N}_2\text{O}_5$	$< 6.0 \times 10^{-23}$			NIST Kinetic
Gaseous	$\text{CH}_3\text{OH} + \text{NO}_3 \rightarrow \text{CH}_3\text{OH-NO}_3$	$1.3 \times 10^{-18}$			NIST Kinetic
Gaseous	$\text{CH}_3\text{OH} + \text{N}_2\text{O}_5 \rightarrow \text{CH}_3\text{OH-N}_2\text{O}_5$	$< 2.0^{-19}$			NIST Kinetic
Particulate	$\text{NO}_3 \rightarrow \text{P}_{(Ar)}\text{-NO}_3$		0.08-0.79, $(1.3-26.1) \times 10^{-3}$ , 0.28-0.22	$(1.82 \pm 0.21) \times 10^{-2}$	Gross, S et al., 2008; 2009; Knopf et al., 2011
Particulate	$\text{N}_2\text{O}_5 \rightarrow \text{P}_{(Ar)}\text{-N}_2\text{O}_5$		$\leq 6.6 \times 10^{-5}$ a, $(3.7-5.8) \times 10^{-5}$ b	$(1.37 \pm 0.15) \times 10^{-5}$	Gross, S et al., 2008; 2009; Knopf et al., 2011
Particulate	$\text{NO}_2 \rightarrow \text{P}_{(Ar)}\text{-NO}_2$		$4.3 \times 10^{-9}$ , $\leq 8.5 \times 10^{-6}$	$\sim 1.42 \times 10^{-8}$	Li et al., 2010; Gross, S et al., 2008
Particulate	$\text{HNO}_3 \rightarrow \text{P}_{(Ar)}\text{-HNO}_3$		$\leq 2.5 \times 10^{-5}$	$\sim 7.07 \times 10^{-5}$	Gross, S et al., 2008
Wall loss	$\text{NO}_3 \rightarrow \text{wall}$			$0.031 \pm 0.015$	This study
Wall loss	$\text{N}_2\text{O}_5 \rightarrow \text{wall}$			$0.022 \pm 0.011$	This study

Note: Only first-step reactions were considered,  $\text{CH}_3\text{CN-NO}_3$  and  $\text{CH}_3\text{OH-NO}_3$  simply indicate the class of  $\text{NO}_3$  reaction products with gaseous acetonitrile and methanol.  $\text{P}_{(Ar)}$  represent aromatic-specific particles. NIST kinetics can be sourced: <https://kinetics.nist.gov/kinetics/index.jsp>

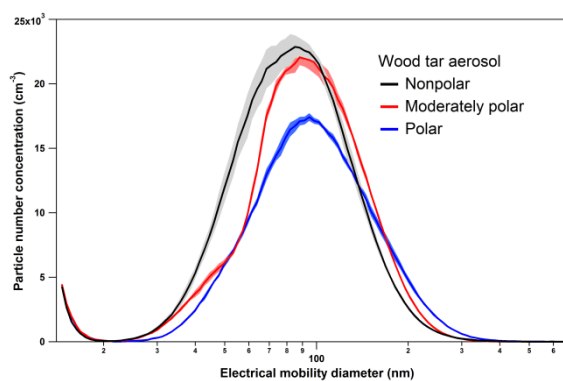


**Figure S3.** Size distribution for initial nonpolar, moderately polar, and polar wood tar aerosols in the aerosol flow tube reactor

A complex pathway simulator (COPASI, <http://copasi.org/>) was used to perform the simulation. The box-model time traces of molecular concentrations for  $N_2O_5$ ,  $NO_3$  radical, wood tar aerosol surface uptake of  $NO_3$  and  $N_2O_5$  are displayed in Figure S4. It is noteworthy that the rapid conversion of  $N_2O_5$  and surface uptake of  $NO_3$  and  $N_2O_5$  within their retention time (165s) occurred in the AFR, and surface uptake of  $NO_3$  radicals by wood tar aerosols exceeds by one or two orders of magnitudes compared to the uptake of  $N_2O_5$ . We therefore concluded that  $NO_3$  radical reactions should be the dominant pathway to oxidize wood tar aerosols, though  $N_2O_5$  can also be nitrating agent at dehydrated organic surface.

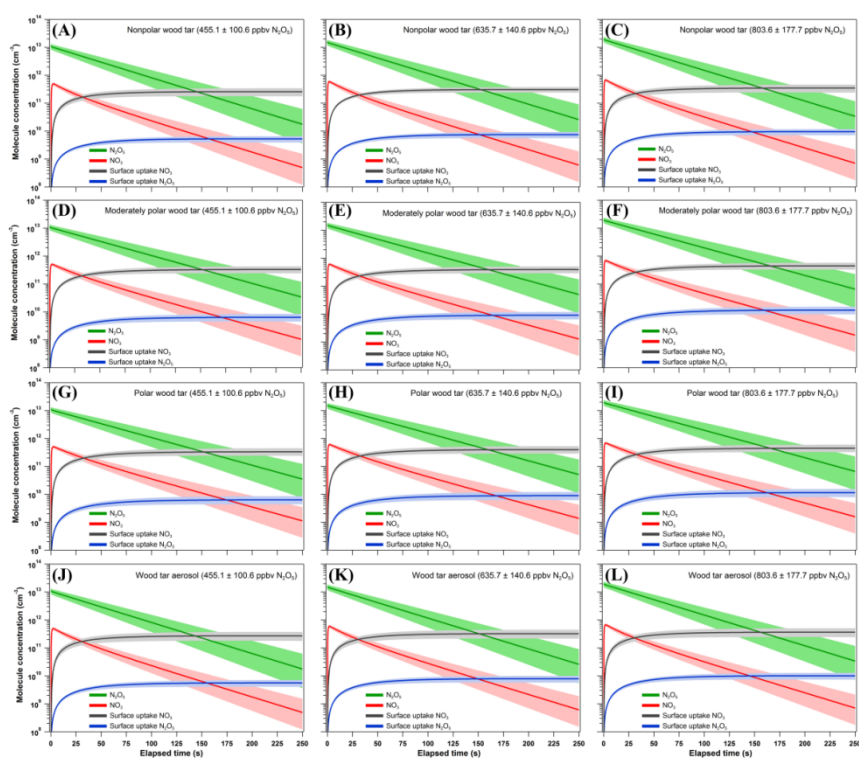


**Figure S4.** Box model time traces of molecular concentrations for  $N_2O_5$ ,  $NO_3$  radical, and surface uptake of  $NO_3$  and  $N_2O_5$  as a function of wood tar particle polarity and initial  $N_2O_5$  concentration. (A)-(C) nonpolar wood tar aerosol, (D)-(F) moderately polar wood tar aerosol, (G)-(I) polar wood tar aerosol, (J)-(L) average result for wood tar aerosol as a function of initial  $N_2O_5$  concentration in the range of 455-804 ppbv.

**S6.2. Quantification of nighttime smoke particle  $NO_3$  aging.** The  $NO_3$  mixing ratios measured *in situ* in urban and rural areas have a large variance, and at ground level in cities and suburban areas next to power plants, the  $NO_3$  concentration may be below the detection limits (0.5-10 pptv) of most instruments due to the high mixing ratio of  $NO$  and or severe particle pollution. At rural areas and forest environments or away from urban areas,  $NO_3$  mixing ratios can reach up to several hundred pptv and  $N_2O_5$  up to a few ppbv.<sup>6,39,40</sup> Though in polluted environments, such as regions influenced by a fire, where  $NO_3$  radical and  $N_2O_5$  have an ultra-low steady-state concentration, the reaction between  $O_3$  and  $NO_2$  in high concentrations can maintain a rapid formation rate for  $NO_3$  radicals, which can be up to several ppbv  $hr^{-1}$ .<sup>41,42</sup> Moreover, the gaseous pollutants from biomass burning can act as a major  $NO_3$  radical sink at nighttime and less than 1% of  $NO_3/N_2O_5$  loss is due to uptake by the smoke aerosol.<sup>41</sup>

To compare with field smoke particle aging due to  $NO_3$  and  $N_2O_5$  reactions, the  $NO_3/N_2O_5$  chemistry in the aerosol flow tube was

quantified as equivalent ambient nighttime NO<sub>3</sub>/N<sub>2</sub>O<sub>5</sub> reactions (*EAN*). We estimated the uptake of NO<sub>3</sub> and N<sub>2</sub>O<sub>5</sub> by wood tar particle downstream of the AFR (RT~165) via the above chemical box model simulation. The uptake of the two species were then normalized to wood tar particle surface area density via:

$$P_{NO_3} = \frac{[NO_3]_{upt} + [N_2O_5]_{upt}}{S} \quad S\ 2\ 5$$

Where  $[NO_3]_{upt}$  and  $[N_2O_5]_{upt}$  are surface uptake of NO<sub>3</sub> and N<sub>2</sub>O<sub>5</sub> from Figure S4, respectively.  $S$  is the wood tar particle surface area density,  $P_{NO_3}$  is the normalized surface uptake of NO<sub>3</sub> and N<sub>2</sub>O<sub>5</sub> as bulk.

According to Decker et al. and Steven S.B. et al.,<sup>41,42</sup> a simple equilibrium between ambient NO<sub>3</sub> radical sink and source in fire plumes within the residual layer can be built with assumption of a steady state for both NO<sub>3</sub> and N<sub>2</sub>O<sub>5</sub>:

$$k_{NO_2-O_3}[NO_2][O_3] \approx \sum_i k_{NO_3-VOC_i}[VOC_i][NO_3] + k_{NO_3}^{aerosol}[NO_3] \quad S\ 2\ 6$$

$$k_{NO_3}^{aerosol} = K_{eq}[NO_2]k_{N_2O_5-aerosol} + k_{NO_3-aerosol} \quad S\ 2\ 7$$

Where the left part of Equation S26 is NO<sub>3</sub> radical production rate from reaction of NO<sub>2</sub> and O<sub>3</sub>, the right side is instant NO<sub>3</sub> radical consumption via homogeneous reactions with VOCs and smoke particle surface uptake. Equation S27 depicts NO<sub>3</sub> radical and N<sub>2</sub>O<sub>5</sub> uptake to particle surface. The estimated NO<sub>3</sub> radical reactivity due to homogeneous biomass burning VOCs reaction is a factor of 100-1000 greater than smoke aerosol surface uptake in fresh emissions.<sup>41</sup> Considering the rapid aging, dilution, and smoke particle growth due to condensation and coagulation during biomass burning emissions transport, the NO<sub>3</sub> radical reactivity due to surface uptake should weigh more in the total reactivity. Here we assumed a median and constant ratio of 500 for total NO<sub>3</sub> reactivity to smoke particle uptake during nighttime atmospheric process:

$$\sum_i k_{NO_3-VOC_i}[VOC_i] + k_{NO_3}^{aerosol} \approx 500 \times k_{NO_3}^{aerosol} \quad S\ 2\ 8$$

Normalize the NO<sub>3</sub> radical uptake rate to smoke particle surface area:

$$R_{NO_3}^{aerosol} = \frac{k_{NO_3}^{aerosol}[NO_3]}{S_{aerosol}} \approx \frac{k_{NO_2-O_3}[NO_2][O_3]}{500 \times S_{aerosol}} \quad S\ 2\ 9$$

Where  $R_{NO_3}^{aerosol}$  is the smoke particle surface area normalized NO<sub>3</sub> radical uptake rate,  $S_{aerosol}$  is surface area density for ambient smoke aerosol. Then the AFR reaction between NO<sub>3</sub>-N<sub>2</sub>O<sub>5</sub> and wood tar particles can be quantified to practical aging time for field fire emissions at nighttime, termed as “equivalent ambient nighttime NO<sub>3</sub>/N<sub>2</sub>O<sub>5</sub> reaction (*EAN*)” combining Equation S25 and S29:

$$EAN = \frac{P_{NO_3}}{R_{NO_3}^{aerosol}} = \frac{P_{NO_3} \times 500 \times S_{aerosol}}{k_{NO_2-O_3}[NO_2][O_3]} \quad S\ 3\ 0$$

The ambient NO<sub>2</sub> and O<sub>3</sub> are commonly in the range of 10-50 ppbv in field fire influenced regions or next to the fire plumes, while smoke particles have practical concentrations with average PM<sub>2.5</sub> within 50 μg m<sup>-3</sup> at nighttime.<sup>41-43</sup> In this study, typical ambient NO<sub>2</sub>, O<sub>3</sub>, and smoke particle surface density were taken as 25 ppbv, 35 ppbv, and 2×10<sup>8</sup> nm<sup>2</sup> cm<sup>-3</sup>, respectively, referring to reference and also our previous work.<sup>41-43</sup> The estimated *EAN* under such condition were estimated for wood tar particles and presented in Table S4.

**Table S4.** Chemical-box model estimated equivalent ambient NO<sub>3</sub> radical aging time for wood tar particles

Initial N <sub>2</sub> O <sub>5</sub> density (ppbv)	Wood tar aerosol (EAN: h)			
	Nonpolar	Moderately polar	Polar	Average
455.1 ± 100.6	7.52 ± 2.16	9.37 ± 3.19	8.64 ± 3.03	8.26 ± 2.33
635.7 ± 140.6	10.61 ± 2.57	13.42 ± 3.79	12.17 ± 3.60	11.66 ± 2.74
803.6 ± 177.7	12.05 ± 2.91	15.36 ± 4.28	13.87 ± 4.07	13.26 ± 3.09

**Table S5.** Summarized HR-ToF-AMS results for fresh and NO<sub>3</sub> oxidized wood tar aerosols

<b>Wood tar aerosol</b>	<b>O:C</b>	<b>H:C</b>	<b>N:C</b>	<b><i>f</i><sub>NO3</sub></b>	<b><i>f</i><sub>m/z&gt;100</sub></b>
Polar wood tar_fresh	0.528 ± 0.006	1.773 ± 0.006	0.003 ± 0.002	0.4 wt.%	5.5 wt.%
8.26 ± 2.33 h <i>EAN</i>	0.614 ± 0.003	1.723 ± 0.005	0.030 ± 0.003	2.7 wt.%	4.3 wt.%
11.66 ± 2.74 h <i>EAN</i>	0.675 ± 0.009	1.719 ± 0.004	0.056 ± 0.004	4.6 wt.%	4.3 wt.%
13.26 ± 3.09 h <i>EAN</i>	0.716 ± 0.006	1.714 ± 0.006	0.084 ± 0.002	6.7 wt.%	4.2 wt.%
Moderately polar wood tar_fresh	0.312 ± 0.006	1.633 ± 0.006	0.002 ± 0.002	0.4 wt.%	25.2 wt.%
8.26 ± 2.33 h <i>EAN</i>	0.368 ± 0.012	1.614 ± 0.005	0.021 ± 0.001	2.2 wt.%	20.6 wt.%
11.66 ± 2.74 h <i>EAN</i>	0.433 ± 0.007	1.604 ± 0.008	0.047 ± 0.001	4.7 wt.%	18.3 wt.%
13.26 ± 3.09 h <i>EAN</i>	0.468 ± 0.010	1.600 ± 0.004	0.076 ± 0.002	7.2 wt.%	15.3 wt.%
Nonpolar wood tar_fresh	0.186 ± 0.005	1.568 ± 0.006	0.000 ± 0.000	0.1 wt.%	32.9 wt.%
8.26 ± 2.33 h <i>EAN</i>	0.273 ± 0.005	1.563 ± 0.007	0.026 ± 0.002	3.0 wt.%	26.7 wt.%
11.66 ± 2.74 h <i>EAN</i>	0.338 ± 0.004	1.533 ± 0.005	0.048 ± 0.004	5.1 wt.%	27.1 wt.%
13.26 ± 3.09 h <i>EAN</i>	0.389 ± 0.007	1.528 ± 0.008	0.094 ± 0.004	9.4 wt.%	24.6 wt.%

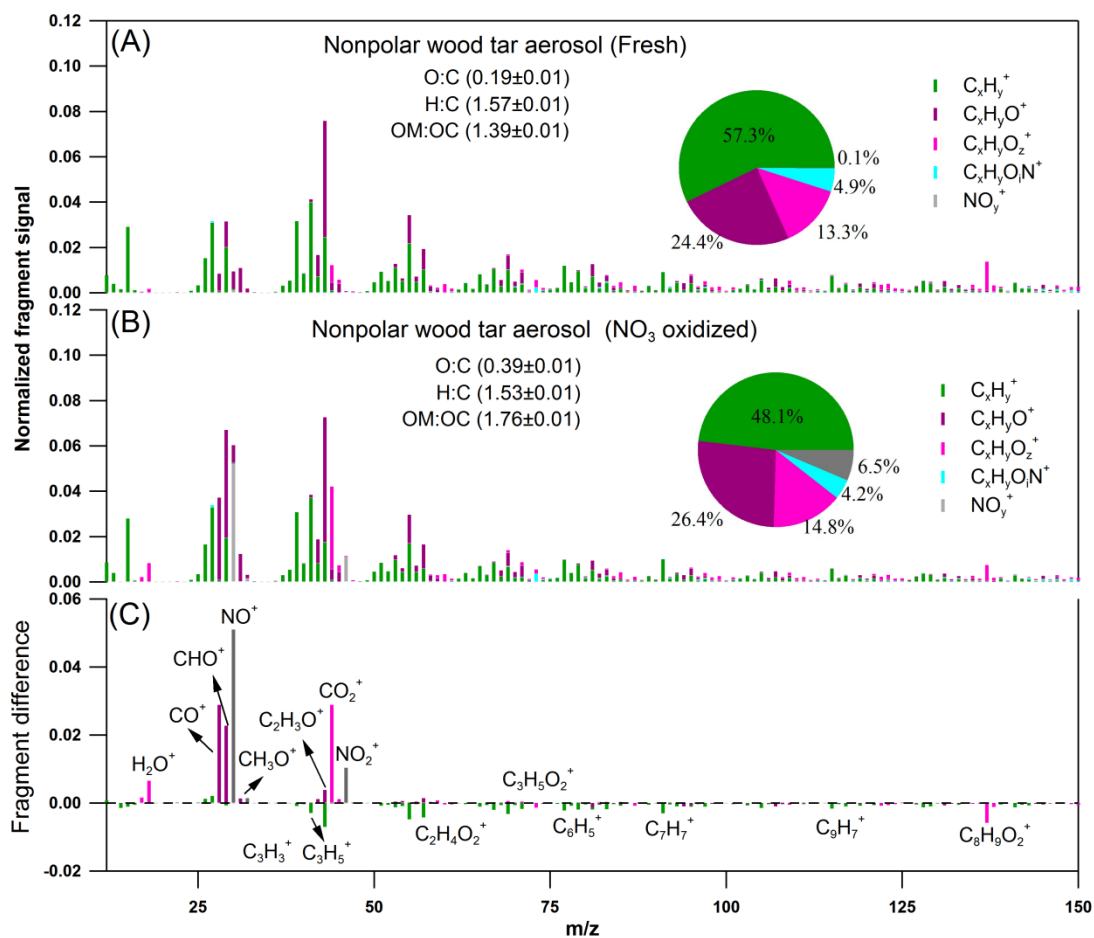


**Figure S5.** Comparison of AMS result for nonpolar wood tar aerosol before (A) and after 13.3 h equivalent ambient NO<sub>3</sub> radical oxidation (B). The mass spectra difference was presented in (C). Five groups were classified based on fragment elemental compositions, e.g., C<sub>x</sub>H<sub>y</sub><sup>+</sup>, C<sub>x</sub>H<sub>y</sub>O<sup>+</sup>, C<sub>x</sub>H<sub>y</sub>O<sub>z</sub><sup>+</sup>, C<sub>x</sub>H<sub>y</sub>O<sub>i</sub>N<sup>+</sup>, and NO<sub>y</sub><sup>+</sup>, where  $x \geq 1$ ,  $y \geq 1$ ,  $z > 1$ ,  $i \geq 0$ . H<sub>x</sub>O<sub>y</sub><sup>+</sup> fragments were grouped in C<sub>x</sub>H<sub>y</sub>O<sub>z</sub><sup>+</sup>. Mass fractions of these five groups were shown as inserted pie-chart.

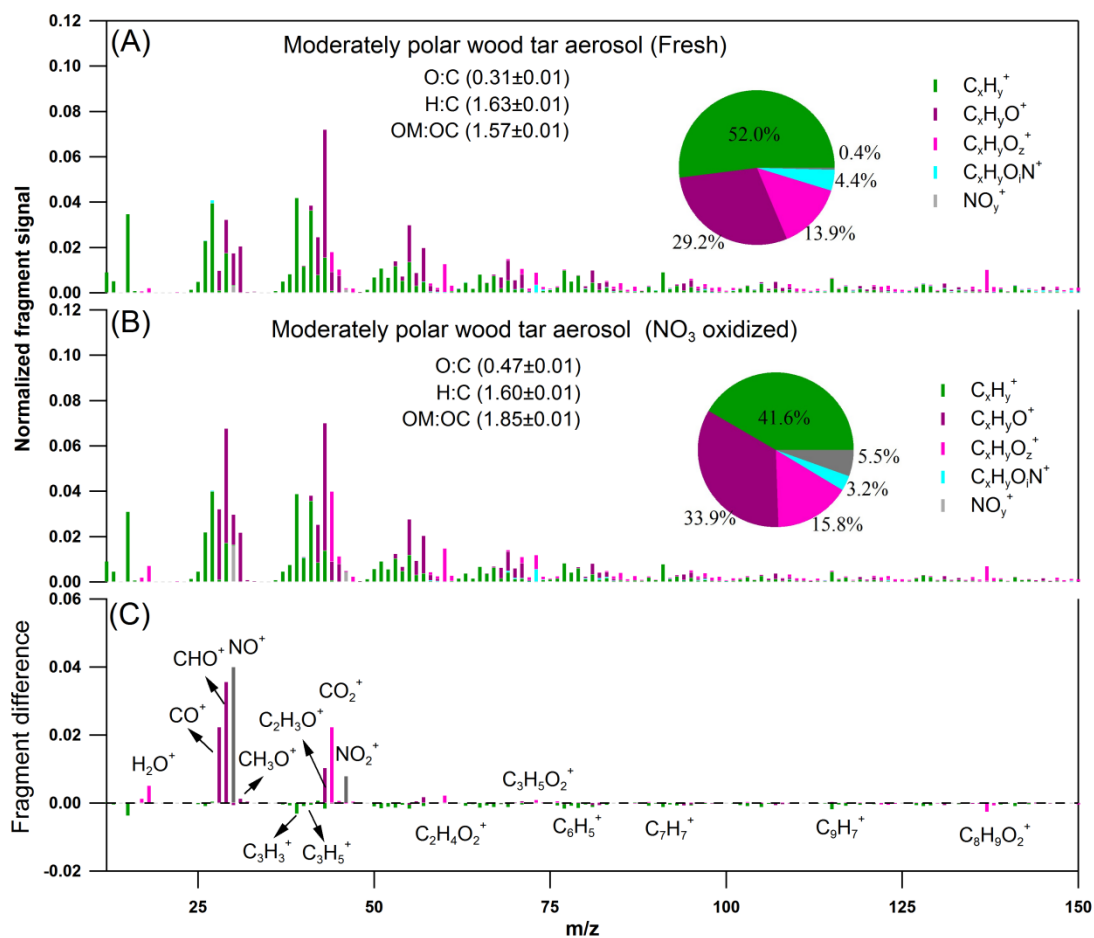


**Figure S6.** Comparison of AMS result for wood tar aerosol with moderate polarity before (A) and after 13.3 h equivalent ambient NO<sub>3</sub> radical oxidation (B). The mass spectra difference was presented in (C). Five groups were classified based on fragment elemental compositions, e.g., C<sub>x</sub>H<sub>y</sub><sup>+</sup>, C<sub>x</sub>H<sub>y</sub>O<sup>+</sup>, C<sub>x</sub>H<sub>y</sub>O<sub>z</sub><sup>+</sup>, C<sub>x</sub>H<sub>y</sub>O<sub>i</sub>N<sup>+</sup>, and NO<sub>y</sub><sup>+</sup>, where x≥1, y≥1, z>1, i≥0. H<sub>x</sub>O<sub>y</sub><sup>+</sup> fragments were grouped in C<sub>x</sub>H<sub>y</sub>O<sub>z</sub><sup>+</sup>. Mass fractions of these five groups were shown as inserted pie-chart.

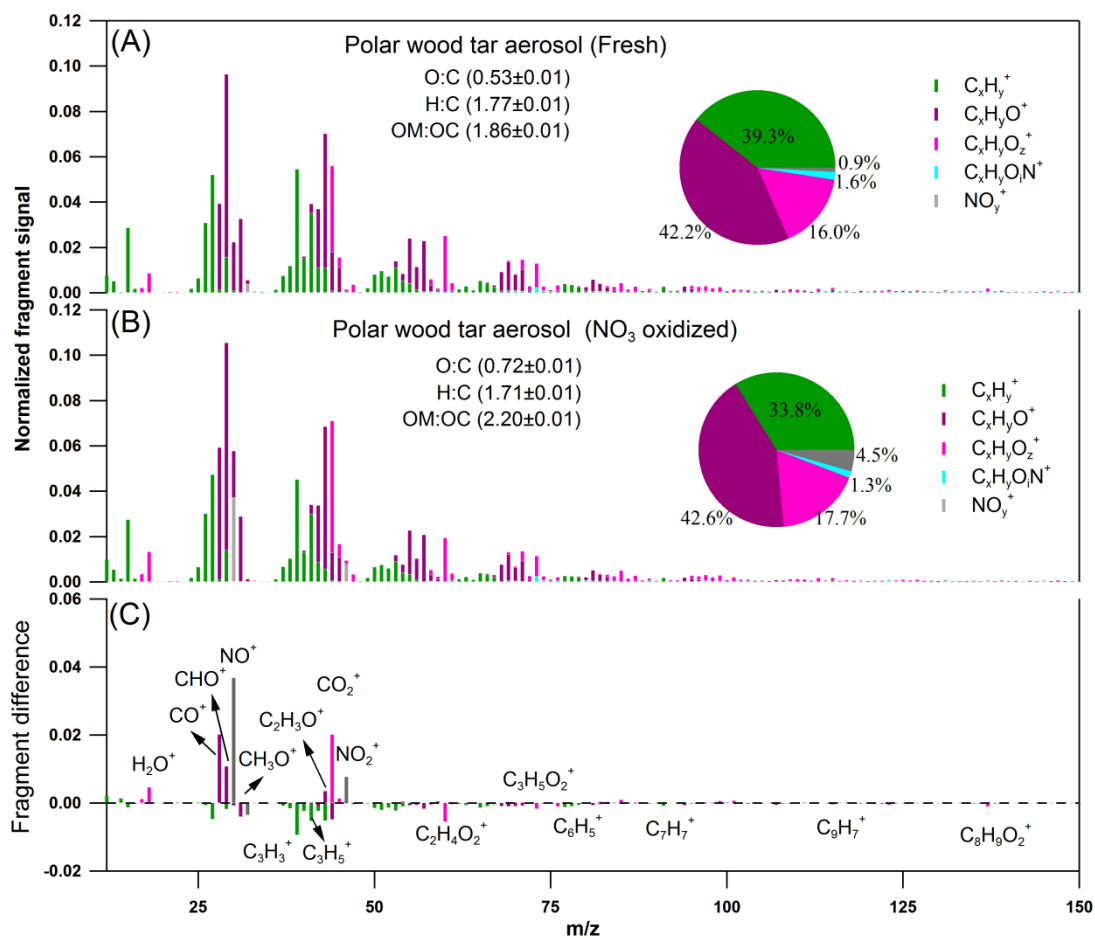


**Figure S7.** Comparison of AMS result for polar wood tar aerosol before (A) and after 13.3 h equivalent ambient NO<sub>3</sub> radical oxidation (B). The mass spectra difference was presented in (C). Five groups were classified based on fragment elemental compositions, e.g., C<sub>x</sub>H<sub>y</sub><sup>+</sup>, C<sub>x</sub>H<sub>y</sub>O<sup>+</sup>, C<sub>x</sub>H<sub>y</sub>O<sub>z</sub><sup>+</sup>, C<sub>x</sub>H<sub>y</sub>O<sub>z</sub>N<sup>+</sup>, and NO<sub>y</sub><sup>+</sup>, where  $x \geq 1$ ,  $y \geq 1$ ,  $z > 1$ ,  $i \geq 0$ . H<sub>x</sub>O<sub>y</sub><sup>+</sup> fragments were grouped in C<sub>x</sub>H<sub>y</sub>O<sub>z</sub><sup>+</sup>. Mass fractions of these five groups were shown as inserted pie-chart.

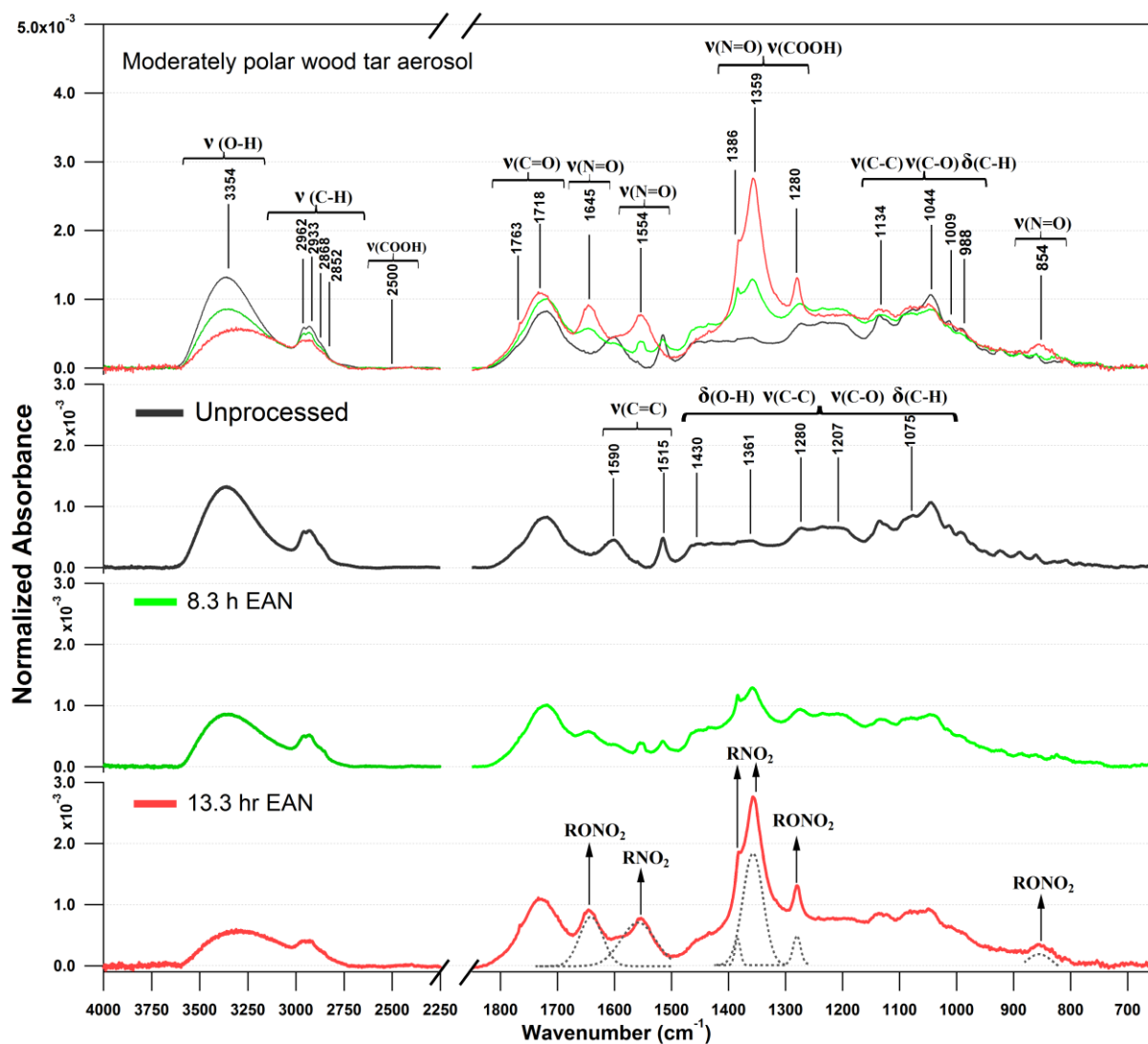


**Figure S8.** FT-IR spectra for moderately polar wood tar particles as a function of  $\text{NO}_3$  radical exposure. The signal was normalized to the entire spectral area. Therefore, the formation of new functional groups can be directly inferred from the appearance of new peaks, while variations in the original functional groups can be inferred by changes in the signals of the parent functional groups.

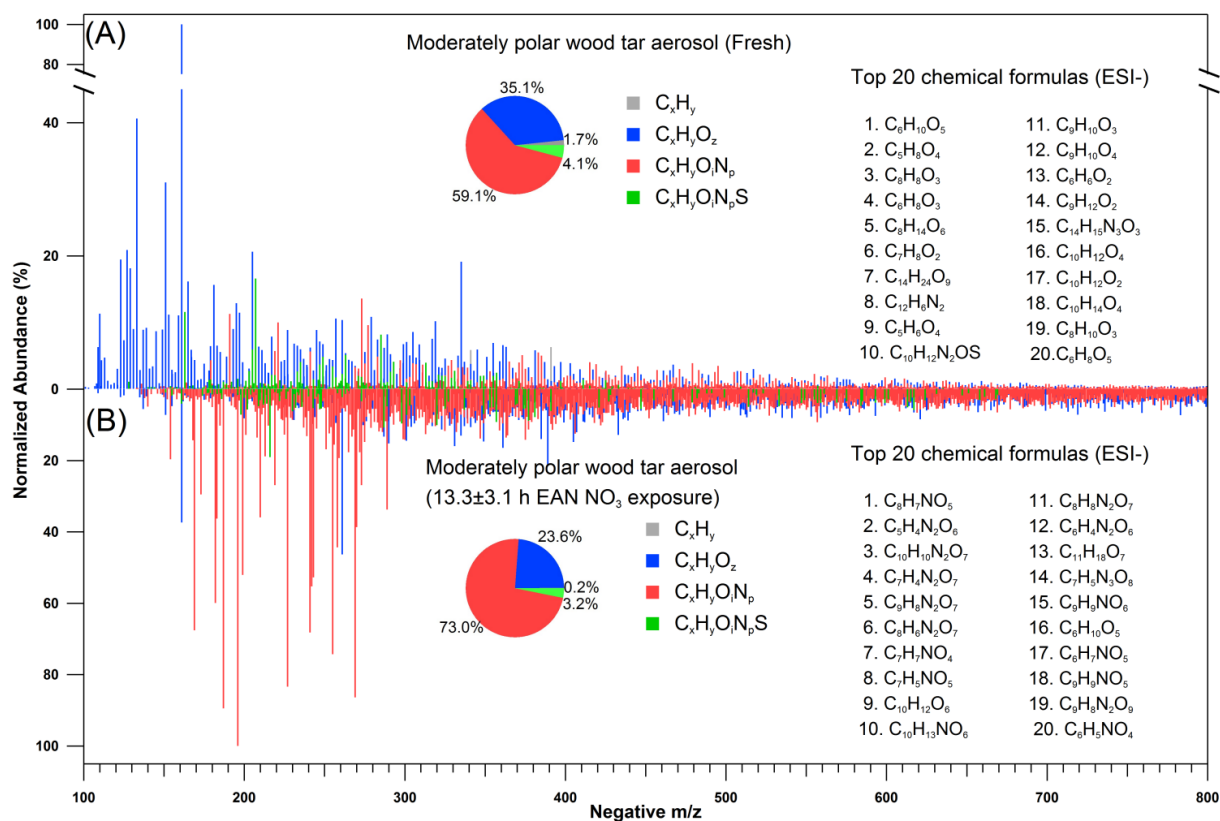


**Figure S9.** High-resolution negative ion mode mass spectra of moderately polar wood tar aerosol obtained before and after 13.3 h equivalent ambient NO<sub>3</sub> radical reaction. The spectra are normalized with respect to the highest intensity of identified molecule. Four chemical groups were classified based on their elemental compositions as C<sub>x</sub>H<sub>y</sub>, C<sub>x</sub>H<sub>y</sub>O<sub>z</sub>, C<sub>x</sub>H<sub>y</sub>O<sub>i</sub>N<sub>p</sub>, C<sub>x</sub>H<sub>y</sub>O<sub>i</sub>N<sub>p</sub>S, where x≥2, y≥2, z≥1, i≥0, and p≥0, respectively. The relative contributions of the four parent chemical groups which constitute the skeletal for all the identified molecules. On the right, 20 identified molecular formulas, obtained with the highest intensity, are shown.

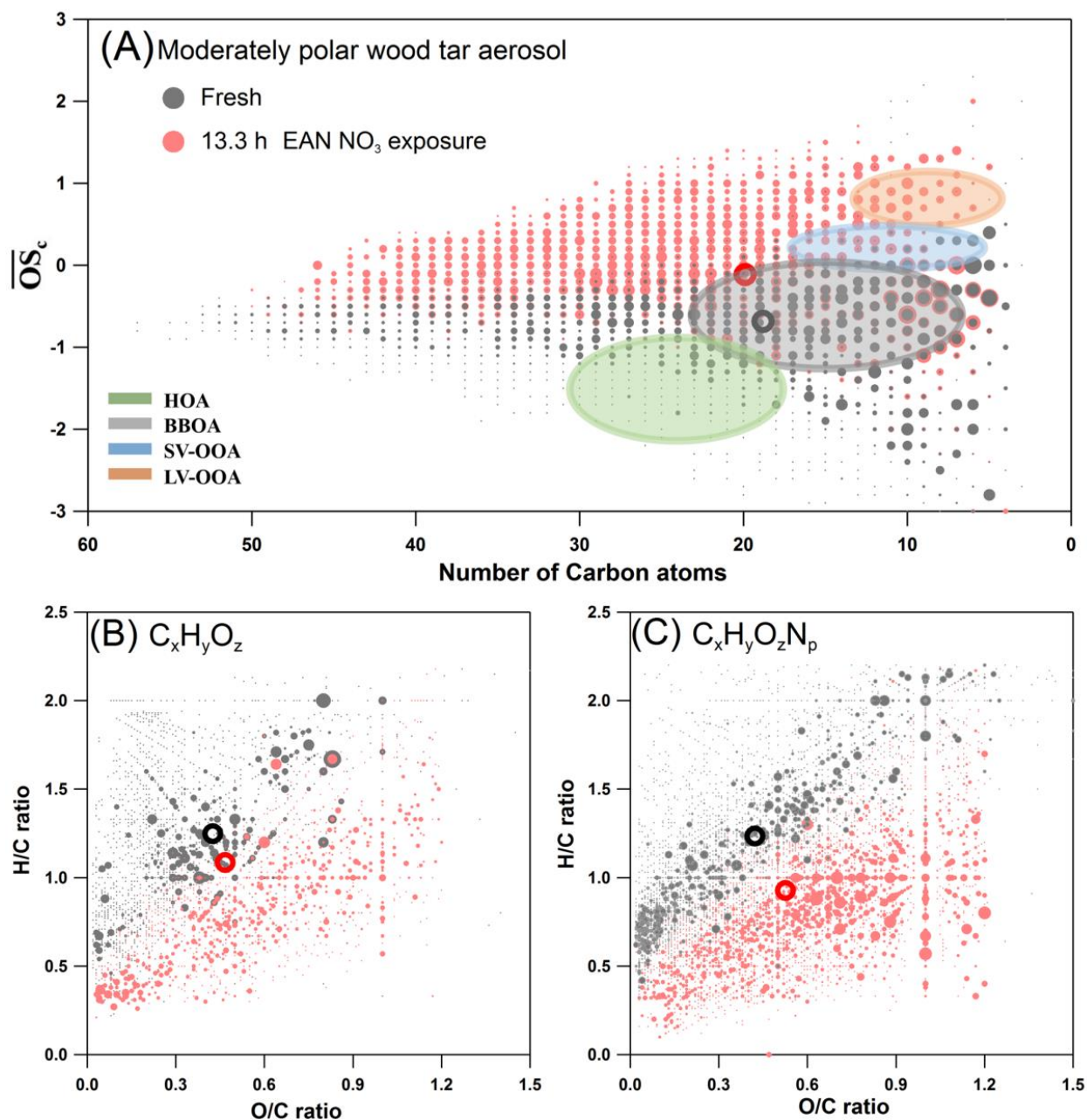


**Figure S10.** Comparison of molecular characteristics of moderately polar wood tar aerosol before and after 13.3 h of EAN NO<sub>3</sub> radical reaction. (A) carbon oxidation state ( $\overline{OS}_c \approx 2 \times O/C - H/C - 5 \times N/C$ ) as a function of molecular carbon number ( $n_c$ ), (B)-(C) Van Krevelen plots of H/C and O/C ratios, for the identified molecule formula from direct infusion (-)ESI-HRMS measurement. The size of the dots indicates the relative intensity obtained for each molecular ion. Characteristic  $\overline{OS}_c - n_c$  for primarily emitted hydrocarbon-like organic aerosol (HOA) and biomass burning organic aerosol (BBOA) were located in light green and gray regions in (A), characteristic  $\overline{OS}_c - n_c$  for semivolatile and low-volatile organic aerosol (SV-OOA and LV-OOA) corresponded to “fresh” and “aged” secondary aerosol produced by secondary oxidation were grouped in light indigo and orange regions in (A).<sup>44</sup> Open dot was ion intensity weighted average elemental ratio corresponding to each group.

**Table S6.** Average elemental composition, elemental ratios, and carbon oxidation state ( $\overline{\delta S}$ ) for moderately polar wood tar aerosol before and after 13.3 h equivalent ambient  $\text{NO}_3$  radical reaction. Results were derived from (-) ESI-HRMS measurements.

Elemental characteristic	$\langle \text{C} \rangle$	$\langle \text{H} \rangle$	$\langle \text{O} \rangle$	$\langle \text{N} \rangle$	$\langle \text{S} \rangle$	$\langle \text{H/C} \rangle$	$\langle \text{O/C} \rangle$	$\langle \text{N/C} \rangle$	$\langle \overline{\delta S} \rangle$
Unprocessed	18.60	22.75	5.79	0.68	0.07	1.22	0.31	0.04	-0.80
$\text{NO}_3$ radical reacted	20.58	21.56	9.69	1.32	0.02	1.05	0.47	0.06	-0.41
difference	1.98	-1.19	3.90	0.64	-0.05	-0.17	0.16	0.02	0.39

Note: These signal intensity weighted average molecular information was obtained by assuming unified response of different compounds. However, different organic compounds might have different sensitivities in the (-) ESI-HRMS. Thus, uncertainties exist when we use the ion intensities for calculating average molecular information.

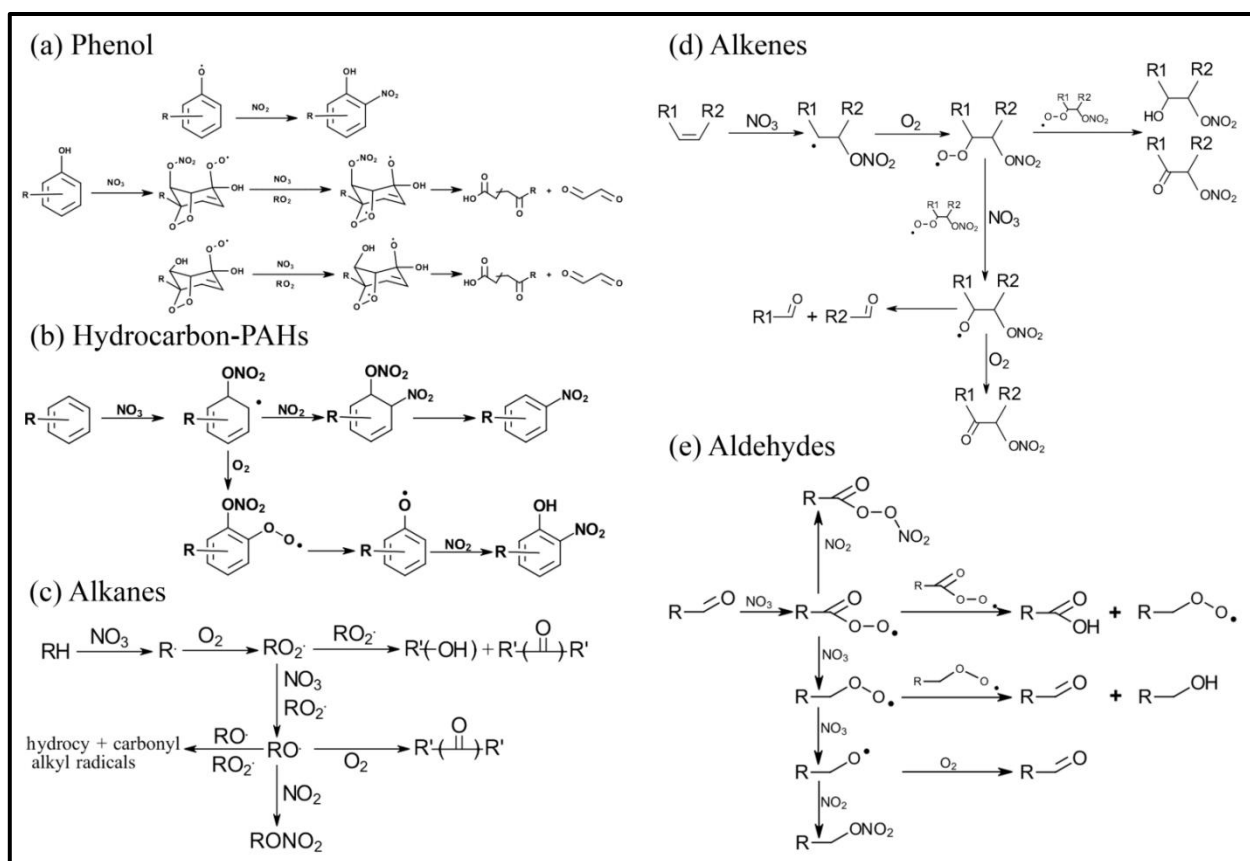


**Figure S11.** Proposed mechanism for  $\text{NO}_3$  radical reactions of organic family that were identified in wood tar aerosols in presence of  $\text{NO}_2$  and  $\text{O}_2$  with organic family that were identified in wood tar aerosol. All schematic reaction pathways were extracted from MCM (<http://mcm.leeds.ac.uk/MCMv3.3.1/roots.htm>) and related publications,<sup>23,35,45,46</sup> only some main reaction pathways were included.

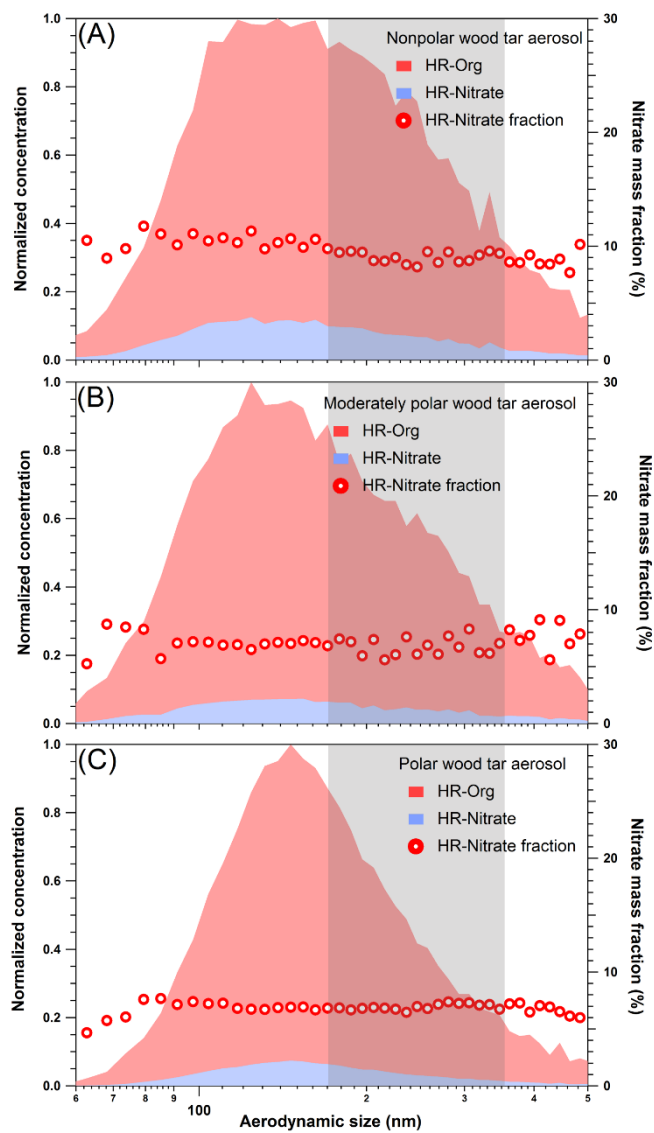


**Figure S12.** HR-ToF-AMS measured chemical composition and nitrate mass fraction as a function of particle size for  $\text{NO}_3$  radical reacted wood tar aerosols (13.3 hr EAN).

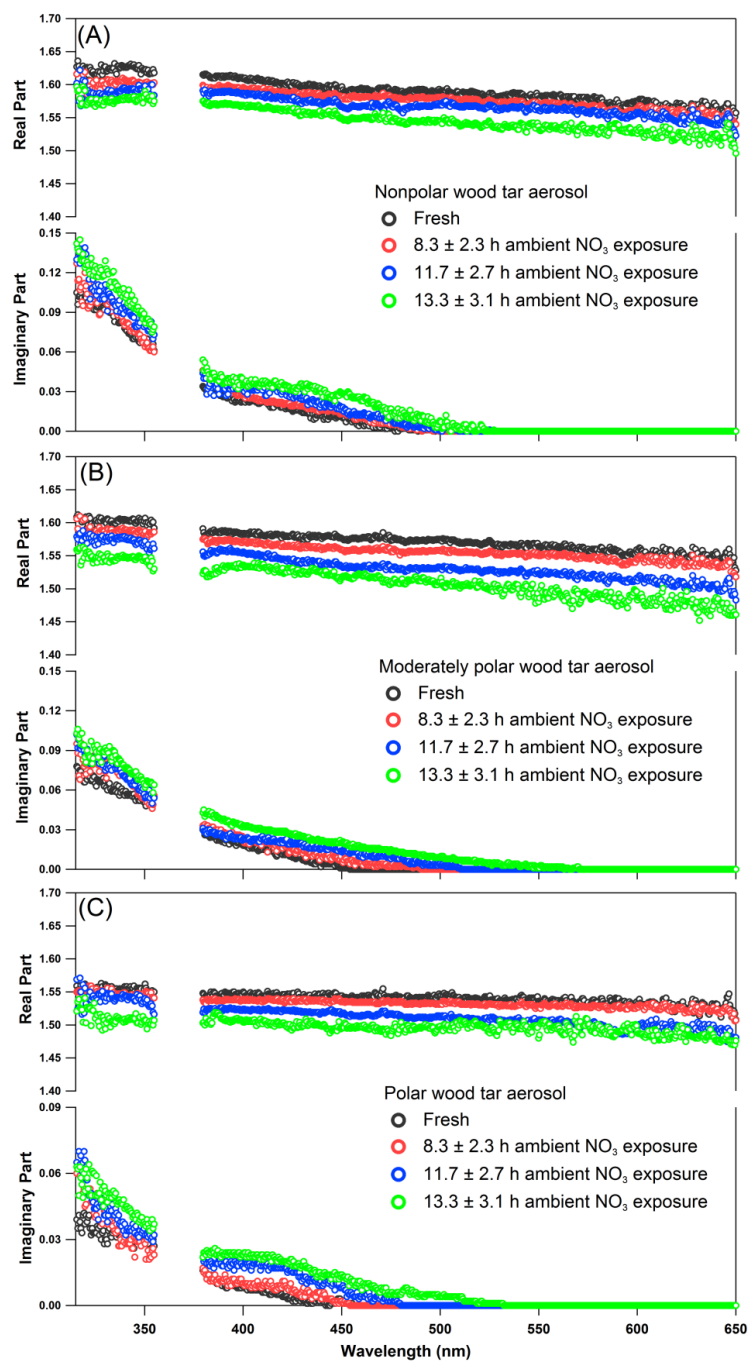


**Figure S13.** Retrieved broadband complex RIs as a function of wavelength (315-355 and 385-650 nm) and NO<sub>3</sub> radical aged degree (fresh to 13.3 hr equivalent field NO<sub>3</sub> radical oxidation at night) for: (A) nonpolar, (B) moderately polar, and (C) polar wood tar aerosols. For clarity, the error bar ( $\pm 0.006$  for real part and  $\pm 0.003$  for imaginary part on average) for the retrieved RI are not shown, and can be found in the supporting information excel file.

## References

- (1) Tóth, A.; Hoffer, A.; Nyirő-Kósa, I.; Pósfai, M.; Gelencsér, A., Atmospheric tar balls: aged primary droplets from biomass burning? *Atmos. Chem. Phys.* **2014**, *14*, (13), 6669-6675.
- (2) Li, C.; He, Q.; Schade, J.; Passig, J.; Zimmermann, R.; Laskin, A.; Rudich, Y., Dynamic changes of optical and chemical properties of tar ball aerosols by atmospheric photochemical aging. *Atmos. Chem. Phys.* **2019**, *2019*, (19), 139-163.
- (3) He, Q.; Bluvshstein, N.; Segev, L.; Meidan, D.; Flores, J. M.; Brown, S. S.; Brune, W.; Rudich, Y., Evolution of the complex refractive index of secondary organic aerosols during atmospheric aging. *Environ. Sci. Technol.* **2018**, *52*, (6), 3456-3465.
- (4) Riziq, A. A.; Rudich, Y., Progress in the investigation of aerosols' optical properties using cavity ring-down spectroscopy. *Fundamentals and Applications in Aerosol Spectroscopy* **2010**, 269.
- (5) Berden, G.; Engeln, R., Cavity ring-down spectroscopy: techniques and applications. John Wiley & Sons: 2009.
- (6) Brown, S.; Stark, H.; Ravishankara, A., Cavity ring-down spectroscopy for atmospheric trace gas detection: application to the nitrate radical (NO<sub>3</sub>). *Appl. Phys. B* **2002**, *75*, (2-3), 173-182.
- (7) Tavakoli, F.; Olfert, J. S., Determination of particle mass, effective density, mass-mobility exponent, and dynamic shape factor using an aerodynamic aerosol classifier and a differential mobility analyzer in tandem. *J. Aerosol Sci.* **2014**, *75*, 35-42.
- (8) Tavakoli, F.; Olfert, J., An instrument for the classification of aerosols by particle relaxation time: theoretical models of the aerodynamic aerosol classifier. *Aerosol Sci. Technol.* **2013**, *47*, (8), 916-926.
- (9) Nir Bluvshstein, J. M. F., Lior Segev, Yinon Rudich, A new approach for retrieving the UV-vis optical properties of ambient aerosols. *Atmos. Meas. Tech.* **2016**, *9*, (8), 3477.
- (10) Washenfelder, R.; Flores, J.; Brock, C.; Brown, S.; Rudich, Y., Broadband measurements of aerosol extinction in the ultraviolet spectral region. *Atmos. Meas. Tech.* **2013**, *6*, (4), 861-877.
- (11) Adler, G.; Riziq, A. A.; Erlick, C.; Rudich, Y., Effect of intrinsic organic carbon on the optical properties of fresh diesel soot. *Proc. Natl. Acad. Sci. U. S. A.* **2010**, *107*, (15), 6699-6704.
- (12) Flores, J. M.; Trainic, M.; Borrmann, S.; Rudich, Y., Effective broadband refractive index retrieval by a white light optical particle counter. *Phys. Chem. Chem. Phys.* **2009**, *11*, (36), 7943-7950.
- (13) Lu, J. W.; Flores, J. M.; Lavi, A.; Abo-Riziq, A.; Rudich, Y., Changes in the optical properties of benzo[a]pyrene-coated aerosols upon heterogeneous reactions with NO<sub>2</sub> and NO<sub>3</sub>. *Phys. Chem. Chem. Phys.* **2011**, *13*, (14), 6484-6492.
- (14) Aiken, A. C.; Decarlo, P. F.; Kröll, J. H.; Worsnop, D. R.; Huffman, J. A.; Docherty, K. S.; Ulbrich, I. M.; Mohr, C.; Kimmel, J. R.; Sueper, D., O/C and OM/OC ratios of primary, secondary, and ambient organic aerosols with high-resolution time-of-flight aerosol mass spectrometry. *Environ. Sci. Technol.* **2008**, *42*, (12), 4478-4485.
- (15) Jennerwein, M.; Eschner, M.; Wilharm, T.; Gröger, T.; Zimmermann, R., Evaluation of reversed phase versus normal phase column combination for the quantitative analysis of common commercial available middle distillates using GC×GC-TOFMS and Visual Basic Script. *Fuel* **2019**, *235*, 336-338.

- (16) Jennerwein, M. K.; Eschner, M. S.; Wilharm, T.; Zimmermann, R.; Gröger, T. M., Proof of concept of high-temperature comprehensive two-dimensional gas chromatography time-of-flight mass spectrometry for two-dimensional simulated distillation of crude oils. *Energy & Fuels* **2017**, *31*, (11), 11651-11659.
- (17) Bae, E.; Yeo, I. J.; Jeong, B.; Shin, Y.; Shin, K.-H.; Kim, S., Study of double bond equivalents and the numbers of carbon and oxygen atom distribution of dissolved organic matter with negative-mode FT-ICR MS. *Anal. Chem.* **2011**, *83*, (11), 4193-4199.
- (18) Laskin, J.; Laskin, A.; Roach, P. J.; Slysz, G. W.; Anderson, G. A.; Nizkorodov, S. A.; Bones, D. L.; Nguyen, L. Q., High-resolution desorption electrospray ionization mass spectrometry for chemical characterization of organic aerosols. *Anal. Chem.* **2010**, *82*, (5), 2048-2058.
- (19) Lee, H. J.; Aiona, P. K.; Laskin, A.; Laskin, J.; Nizkorodov, S. A., Effect of solar radiation on the optical properties and molecular composition of laboratory proxies of atmospheric brown carbon. *Environ. Sci. Technol.* **2014**, *48*, (17), 10217-10226.
- (20) Lin, P.; Aiona, P. K.; Li, Y.; Shiraiwa, M.; Laskin, J.; Nizkorodov, S. A.; Laskin, A., Molecular characterization of brown carbon in biomass burning aerosol particles. *Environ. Sci. Technol.* **2016**, *50*, (21), 11815-11824.
- (21) Lin, P.; Fleming, L. T.; Nizkorodov, S. A.; Laskin, J.; Laskin, A., Comprehensive Molecular Characterization of Atmospheric Brown Carbon by High Resolution Mass Spectrometry with Electrospray and Atmospheric Pressure Photoionization. *Anal. Chem.* **2018**, *90*, (21), 12493-12502.
- (22) Gross, S.; Iannone, R.; Xiao, S.; Bertram, A. K., Reactive uptake studies of NO<sub>3</sub> and N<sub>2</sub>O<sub>5</sub> on alkenoic acid, alkanolate, and polyalcohol substrates to probe nighttime aerosol chemistry. *Phys. Chem. Chem. Phys.* **2009**, *11*, (36), 7792-7803.
- (23) Gross, S.; Bertram, A. K., Reactive uptake of NO<sub>3</sub>, N<sub>2</sub>O<sub>5</sub>, NO<sub>2</sub>, HNO<sub>3</sub>, and O<sub>3</sub> on three types of polycyclic aromatic hydrocarbon surfaces. *J. Phys. Chem. A* **2008**, *112*, (14), 3104-3113.
- (24) Chang, W. L.; Bhave, P. V.; Brown, S. S.; Riemer, N.; Stutz, J.; Dabdub, D., Heterogeneous atmospheric chemistry, ambient measurements, and model calculations of N<sub>2</sub>O<sub>5</sub>: A review. *Aerosol Sci. Technol.* **2011**, *45*, (6), 665-695.
- (25) Ng, N. L.; Brown, S. S.; Archibald, A. T.; Atlas, E.; Cohen, R. C.; Crowley, J. N.; Day, D. A.; Donahue, N. M.; Fry, J. L.; Fuchs, H., Nitrate radicals and biogenic volatile organic compounds: oxidation, mechanisms, and organic aerosol. *Atmos. Chem. Phys.* **2017**, *17*, (3), 2103-2162.
- (26) Phillips, G. J.; Thieser, J.; Tang, M.; Sobanski, N.; Schuster, G.; Fachinger, J.; Drewnick, F.; Borrmann, S.; Bingemer, H.; Lelieveld, J., Estimating N<sub>2</sub>O<sub>5</sub> uptake coefficients using ambient measurements of NO<sub>3</sub>, N<sub>2</sub>O<sub>5</sub>, ClNO<sub>2</sub> and particle-phase nitrate. *Atmos. Chem. Phys.* **2016**, *16*, 13231-13249.
- (27) Crowley, J.; Ammann, M.; Cox, R.; Hynes, R.; Jenkin, M. E.; Mellouki, A.; Rossi, M.; Troe, J.; Wallington, T., Evaluated kinetic and photochemical data for atmospheric chemistry: Volume V-heterogeneous reactions on solid substrates. *Atmos. Chem. Phys.* **2010**, *10*, (18), 9059-9223.
- (28) Davidovits, P.; Kolb, C. E.; Williams, L. R.; Jayne, J. T.; Worsnop, D. R., Mass accommodation and chemical reactions at gas-liquid interfaces. *Chem. Rev.* **2006**, *106*, (4), 1323-1354.

- (29) Pöschl, U.; Rudich, Y.; Ammann, M., Kinetic model framework for aerosol and cloud surface chemistry and gas-particle interactions-Part 1: General equations, parameters, and terminology. *Atmos. Chem. Phys.* **2007**, *7*, (23), 5989-6023.
- (30) Ammann, M.; Pöschl, U., Kinetic model framework for aerosol and cloud surface chemistry and gas-particle interactions-Part 2: Exemplary practical applications and numerical simulations. *Atmos. Chem. Phys.* **2007**, *7*, (23), 6025-6045.
- (31) Zasytkin, A. Y.; Grigor'eva, V.; Korchak, V.; Gershenson, Y. M., A formula for summing of kinetic resistances for mobile and stationary media: I. Cylindrical reactor. *Kinet. Cat.* **1997**, *38*, (6), 772-781.
- (32) Knopf, D. A.; Forrester, S. M.; Slade, J. H., Heterogeneous oxidation kinetics of organic biomass burning aerosol surrogates by O<sub>3</sub>, NO<sub>2</sub>, N<sub>2</sub>O<sub>5</sub>, and NO<sub>3</sub>. *Phys. Chem. Chem. Phys.* **2011**, *13*, (47), 21050-21062.
- (33) Kolb, C.; Cox, R. A.; Abbatt, J.; Ammann, M.; Davis, E.; Donaldson, D.; Garrett, B. C.; George, C.; Griffiths, P.; Hanson, D., An overview of current issues in the uptake of atmospheric trace gases by aerosols and clouds. *Atmos. Chem. Phys.* **2010**, *10*, (21), 10561-10605.
- (34) George, I.; Abbatt, J., Heterogeneous oxidation of atmospheric aerosol particles by gas-phase radicals. *Nat. Chem.* **2010**, *2*, (9), 713.
- (35) Liu, C.; Zhang, P.; Wang, Y.; Yang, B.; Shu, J., Heterogeneous reactions of particulate methoxyphenols with NO<sub>3</sub> radicals: Kinetics, products, and mechanisms. *Environ. Sci. Technol.* **2012**, *46*, (24), 13262-13269.
- (36) Shiraiwa, M.; Pöschl, U.; Knopf, D. A., Multiphase chemical kinetics of NO<sub>3</sub> radicals reacting with organic aerosol components from biomass burning. *Environ. Sci. Technol.* **2012**, *46*, (12), 6630-6636.
- (37) Tang, M.; Cox, R.; Kalberer, M., Compilation and evaluation of gas phase diffusion coefficients of reactive trace gases in the atmosphere: volume 1. Inorganic compounds. *Atmos. Chem. Phys.* **2014**, *14*, (17), 9233-9247.
- (38) Li, H.; Zhu, T.; Zhao, D.; Zhang, Z.; Chen, Z., Kinetics and mechanisms of heterogeneous reaction of NO<sub>2</sub> on CaCO<sub>3</sub> surfaces under dry and wet conditions. *Atmos. Chem. Phys.* **2010**, *10*, (2), 463-474.
- (39) Khan, M.; Cooke, M.; Utembe, S.; Archibald, A.; Derwent, R.; Xiao, P.; Percival, C.; Jenkin, M.; Morris, W.; Shallcross, D., Global modeling of the nitrate radical (NO<sub>3</sub>) for present and pre-industrial scenarios. *Atmos. Res.* **2015**, *164*, 347-357.
- (40) Asaf, D.; Tas, E.; Pedersen, D.; Peleg, M.; Luria, M., Long-term measurements of NO<sub>3</sub> radical at a semiarid urban site: 2. Seasonal trends and loss mechanisms. *Environ. Sci. Technol.* **2010**, *44*, (15), 5901-5907.
- (41) Decker, Z.; Zarzana, K.; Coggon, M. M.; Min, K.-E.; Pollack, I.; Ryerson, T. B.; Peischl, J.; Edwards, P.; Dubé, W. P.; Markovic, M. Z., Nighttime chemical transformation in biomass burning plumes: a box model analysis initialized with aircraft observations. *Environ. Sci. Technol.* **2019**, *53*, (5), 2529-2538.
- (42) Brown, S. S.; Stutz, J., Nighttime radical observations and chemistry. *Chem. Soc. Rev.* **2012**, *41*, (19), 6405-6447.
- (43) Bluvshstein, N.; Lin, P.; Flores, J. M.; Segev, L.; Mazar, Y.; Tas, E.; Snider, G.; Weagle, C.; Brown, S. S.; Laskin, A., Broadband optical properties of biomass-burning aerosol and identification of brown carbon chromophores. *J. Geophys. Res.: Atmos.* **2017**, *122*, 5441-5456. DOI: 10.1002/2016JD026230.

- (44) Kroll, J. H.; Donahue, N. M.; Jimenez, J. L.; Kessler, S. H.; Canagaratna, M. R.; Wilson, K. R.; Altieri, K. E.; Mazzoleni, L. R.; Wozniak, A. S.; Bluhm, H., Carbon oxidation state as a metric for describing the chemistry of atmospheric organic aerosol. *Nat. Chem.* **2011**, *3*, (2), 133.
- (45) Gross, S.; Bertram, A. K., Products and kinetics of the reactions of an alkane monolayer and a terminal alkene monolayer with NO<sub>3</sub> radicals. *J. Geophys. Res.: Atmos.* **2009**, *114*, (D02307), 1-14. DOI: 10.1029/2008JD010987.
- (46) Docherty, K. S.; Ziemann, P. J., Reaction of oleic acid particles with NO<sub>3</sub> radicals: Products, mechanism, and implications for radical-initiated organic aerosol oxidation. *J. Phys. Chem. A* **2006**, *110*, (10), 3567-3577.